ASSESSING THE POTENTIAL OF ZNO SURFACES

FOR FISCHER-TROPSCH SYNTHESIS

USING CAR-PARRINELLO MOLECULAR DYNAMICS

By

CHARITH R. DESILVA

Bachelor of Science in Physics

Oklahoma State University

Stillwater, OK

2018

Submitted to the Faculty of the
Graduate College of
Oklahoma State University
in partial fulfillment of
the requirements for
the Degree of
MASTERS OF SCIENCE
December, 2020

ASSESSING THE POTENTIAL OF ZNO SURFACES

FOR FISCHER-TROPSCH SYNTHESIS

USING CAR-PARRINELLO MOLECULAR DYNAMICS

Thesis Approved:

Dr. Mario Borunda
_____
Thesis Advisor

Dr. David McIlroy
_____

Dr. Andrew Yost
_____

ACKNOWLEDGMENTS

First I would like to thank my advisor Dr. Mario Borunda, for letting me be a part of his research group and for guiding my progress throughout this project and through my time here at OSU. The knowledge I have gained from my time as a memeber of the Borunda reserach group will be an invaluable learning experiance.

I would also like to thank the members of the Borunda reserach group for supporting me through reserach discussion and general advice about navigating my way through graduate school. In particular, I would like to thank Kyle Stoltz, who helped me though many technical issues that I ran into during this project.

I am also grateful for the faculty and staff in the physics department here at OSU. From undergrad to graduate school, my time here at OSU has shaped me into the person I am today. I am also grateful for all the reserach opportunities that were available to me here at OSU, I have had plently of opportunities to become a better reseracher and I believe that has influenced my charecter greatly.

Lastly, I would like to thank my family and friends. Without their support I would not be where I am today. In particular, I would like to thank Mackenzie Walker. She has supported me though good days and bad, and time spent with her and our many animals was always the best part of finishing a long day.

Name: CHARITH R. DESILVA

Date of Degree: December, 2020

Title of Study: ASSESSING THE POTENTIAL OF ZNO SURFACES FOR FISCHER-TROPSCH SYNTHESIS USING CAR-PARRINELLO MOLECULAR DYNAMICS

Major Field: Physics

Abstract: We investigate the performance of non-polar ZnO surfaces as a catalyst in Fischer-Tropsch synthesis (FTS) through Car-Parrinello molecular dynamics. Economic and environmental concerns regarding the future of fuel production have increased interest in viable FTS catalysts. ZnO nanoparticles are promising catalytic candidates as they are environmentally safe and cost-effective. While the polar-surfaces of ZnO have been heavily studied, the non-polar surfaces have not. We computationally investigate the adsorption properties of various molecules vital to the FTS process over the pristine and defect non-polar ZnO surfaces. All molecular dynamics calculations were carried out with van der Waals exchange-correlation pseudopotentials in order to fully understand the adsorption process. From the results of the molecular dynamics simulations we propose that the ZnO dimer-defect surfaces can absorb and break the bonds of certain molecules, which is vital to the FTS process. We also observed weak interactions between both the dimer and edge-defect surfaces. These results show promise for ZnO defect-surfaces as FTS catalysts and showcase the effectiveness of molecular dynamics in visualizing the adsorption process.

TABLE OF CONTENTS

Chapter   Page

LIST OF TABLES

LIST OF FIGURES

CHAPTER I

Introduction

1.1 Fischer-Tropsch Synthesis

Energy sustainability is one of the most significant issues in modern society. The US Energy Information Administration (EIA) reported in 2013 that global energy consumption would increase by 56 percent between 2010 and 2040 if current economic trends continue[1]. Along with this increase in energy consumption, the EIA estimates that global carbon emissions will increase by 46 percent in the same time frame[1]. Due to these issues and the increasing price of crude oil, there has been considerable effort to reduce the use of petroleum-based fuels[1,2,3]. As a result of these efforts, renewable energy production is increasing significantly with a 2.5 percent increase per year[1]. Even with this increase in renewable energy resources, current predictions state that fossil fuels will supply up to 80 percent of the world's energy by 2040[1].

One approach to combat these issues is to develop materials capable of Fischer-Tropsch synthesis (FTS), which is a catalytic process that converts syngas to energy-storing hydrocarbons[2,3,4]. The FTS process was developed by Franz Fischer and Hans Tropsch in 1926[5]. The first step in that process is coal hydrocracking, which happens by reacting coal with steam which produces a synthesis gas (mix of carbon monoxide and hydrogen). The second step is to convert that synthesis gas into a petroleum-like liquid, which is done in the presence of a cobalt catalyst[5]. This process was highly successful and resulted in the FTS fuels being used to produce 9.1% of Germany's oil supply as early as 1936[6]. In recent years FTS has drawn a lot of attention since creating liquid hydrocarbons from this method is a clean process that can solve the

1

shortage of liquid transport fuels[5].

The FTS process generally includes four chemical reactions as shown in equations 1-4[2;3]. The two main reactions of FTS are shown in equation 1-2; these two reactions produce the energy-storing hydrocarbons used for fuel production. The hydrocarbons produced through these reactions can be sulfur and nitrogen-free, and generally have low aromaticity. Removal of toxic chemicals along with low aromaticity results in fuels made from these chemicals to be environmentally safe and of a higher quality than petroleum-based fuels[2;3]. The side reactions in equations 3-4 showcase the Water-Gas Shift (WGS) reaction and alcohol production[3]. The WGS reaction is critical in FTS since it can balance H2/Co ratios. It can take CO, which is a byproduct of steam reforming reactions, and produce H2 which is used for the main FTS reactions[3;7]. These four chemical reactions in the presence of a catalyst are the basis of FTS.

$$(2n + 1)H_2 + nCO \rightarrow C_nH_{2n+2} + nH_2O \qquad (1.1)$$

$$2nH_2 + nCO \rightarrow C_nH_{2n} + nH_2O \qquad (1.2)$$

$$CO + H_2O \rightarrow CO_2 + H_2 \qquad (1.3)$$

$$2nH_2 + nCO \rightarrow C_nH_{2n+2} + (n - 1)H_2O \qquad (1.4)$$
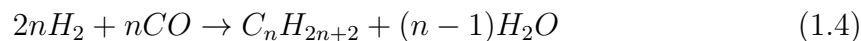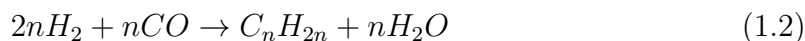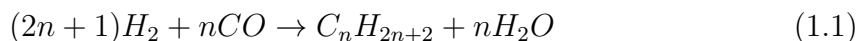
FTS has come a long way since 1936 and has many economic and environmental benefits. Economically, FTS can provide an excellent alternative to crude oil in the form of hydrocarbons[2;3]. This is especially relevant today since it was estimated that the FTS process would be economically preferable over crude oil when oil prices were over US$20 per barrel[2], which has been the case for many years now[1;2]. The environ-

2

mental benefits of FTS are that there are green methods of producing syngas[8;9;10]. One green procedure of producing syngas is through steam and dry reforming of hydrocarbon feedstock and biomass[2;11]. With FTS processes becoming more sustainable and reliable, the next significant effort in FTS research is to find new novel catalysts that are both cost-friendly and environmentally safe.

1.2 Research on FTS and why ZnO as a Catalyst

Environmental and economic concerns regarding the future state of fuel production have resulted in a surge in FTS research in the past decade. This surge has resulted in considerable research on the creation of FTS catalysts with high activation rates[2;4;12;13]. A catalyst is a material that increases the chemical process's reaction rate without being consumed itself[14]. In FTS, the most common catalysts are group VIII materials, namely Cobalt (Co), Ruthenium (Ru), and Iron (Fe)[3;15]. FTS catalysts are not limited to these materials; several other metals have been used including Rhodium and Nickel[2;3]. Among the most common catalysts, Ru is the most active and can work effectively at low temperatures (<150 °C) without the aid of promoters[2]. As an added interest to scientists, Ru catalysts have been shown to produce the highest molecular weight hydrocarbons; however, prohibitive costs and limited resources prevent Ru from being used in industry[2;3;15]. On the other hand, Co and Fe both have lower prices than Ru and have been utilized[2;3]. Fe is the cheapest of the two materials, but Co is generally more active and more resistant to degradation by water[2].

There have also been studies on various promoter materials to improve the activation rates of these FTS catalysts. Promoters added to FTS catalysts can increase the activity of materials by either a structural or electronic change[2]. Unlike Ru, Fe and Co-based catalysts need promoters to reach optimal catalytic performance[2]. The most common types of promoters used with Fe and Co materials are noble metals,

alkali metal ions, and transition metal oxides[2]. Platinum (Pt), Copper (Cu), and Ru are some of the most widely used noble metal promoters; however, many of these metals (Pt and Ru in particular) are expensive to produce[3;12;13;16]. Alkali metal ions like Potassium (K) and Sodium (Na) as well as transition metals oxides such as Magnesium Oxide (MgO) have also been examined as FTS promoters. However, their effectiveness is still debated[2;17]. These two types of promoters increase catalytic activity in some cases, but reduce activity in others[2;17]. One explanation of this is the vast array of different catalyst systems used and the effects of these different modifiers interacting with each other[2;17].

In addition to the research on the promoter effects on commonly used catalysts, there have also been studies on copper-cobalt (CuCo) alloys and[18] and metal oxides like iron-oxide (FeO) and zinc-oxide (ZnO)[19;20] as FTS catalysts. These materials have been studied due to the promising catalytic effects of defects, such as step-sites for CuCo and oxygen vacancies for the metal oxides[18;19]. In particular, ZnO nanoparticles/nanowires are promising since they are environmentally-safe and cost-effective to produce[21]. One green method for producing ZnO nanoparticles is through biosynthesis, where the nanoparticles can be synthesized by using microorganisms and plants. This synthesis method can make ZnO without the excessive use of expensive and toxic chemicals while being renewable[21]. These ZnO surfaces have also been found to have high CO adsorption rates[22;23], which make them prime candidates as an FTS catalyst.

1.3 Defects on ZnO surfaces

Zinc-oxide has many attractive bulk and surface properties, and as a widegap semiconductor, it is a suitable candidate for a variety of applications[24]. However, pristine ZnO surfaces generally do not have sizeable catalytic activities[24;23]. It has been concluded that catalytic activity over pristine ZnO surfaces does not increase with surface

area[24]. These results show that catalysis with ZnO is a structure-sensitive reaction. Structure-sensitive means that defects on the surface and the material's crystalline structure can play a vital role in catalytic activity. Oxygen vacancy defects, in particular, have been found to have a substantial effect on the catalytic activation rates for ZnO[23]. As a result of this finding, the polar (un-stable) surface of ZnO, specifically ZnO $(000\bar{1})$, have been heavily studied[25;26;27].

On the other hand, there has not been much work done on how defects in ZnO surfaces $(10\bar{1}0)$ & $(11\bar{2}0)$ affect activation rates. Through scanning tunneling microscopy (STM) and scanning tunneling spectroscopy (STS) analysis, it was shown that the most likely defect on a $(10\bar{1}0)$ face is a ZnO dimer-defect[22]. It was also discovered that grove and terraces are also commonly found in $(10\bar{1}0)$ & $(11\bar{2}0)$ ZnO surfaces[28]. Knowing the effect of defects on the catalytic activation rates for ZnO, we explore whether the stable ZnO $(10\bar{1}0)$ & $(11\bar{2}0)$ surfaces would make suitable FTS catalysts while investigating the role that dimer defects, groves, and terraces in those surfaces play in the catalysis.

To study the effects of these various defects, calculations of the adsorption properties[3] of syngas need to be performed. Adsorption is the adhesion process of liquid or gas molecules on the surface of a solid[29]. In the case of FTS, the molecules are the syngas and the solid is the catalyst. There are two main types of adsorption, physisorption and chemisorption. Chemisorption is very similar to a traditional chemical bond, while physisorption does not change the chemical structure of the molecule. The fundamental force that guides physisorption is the Van der Waals (VdW) force[29]. This is the crux of my project: to study syngas' adsorption properties on a ZnO catalyst using Density Functional Theory (DFT) while including the VdW interactions. Prior DFT studies have been done at the VdW-corrected level[30;31], but not with molecular dynamics (MD) on ZnO surfaces.

1.4 Molecular Dynamics

Molecular dynamics is a powerful computational technique that is used to study many physical and chemical systems. Here I will use MD to analyze the interactions between syngas and other various molecules with ZnO catalysts. With MD, we can elucidate the kinetics of the adsorption process on ZnO slabs, capturing how the molecules and bonds change over time and the thermodynamics properties of the system[32], which can be used to find where on the ZnO surface adsorption takes place. These MD calculations will not give a complete picture of VdW interactions in adsorption. Still, with MD, we can better understand how these various surface defects in ZnO affect how well these ZnO slabs can be used in the FTS process. In addition to the system's thermodynamic properties, MD can visualize the physical interactions between the syngas and the catalyst in an accessible format. The movies and data taken from the various MD simulations run in this project will showcase these molecules' adsorption properties and give us a good idea of the FTS capabilities of defect ZnO surfaces.

<center>**CHAPTER II**</center>

<center>**Computational Theory and Methodology**</center>

<center>**2.1   The Many-Body Problem**</center>

All of the calculations in this project are done with DFT, and the molecular dynamics simulations use the Car-Parrinello method. In this chapter, I will discuss the theory behind the DFT and DFT-MD and the computational methodology used via the Siesta program[33]. The power of DFT is that it is a method of obtaining the solution for the many-body problem by only using the electron density of the system as a variable. Here we will discuss the many-body problem up to the Hartree-approximation, and then detail how the Kohn-Sham equation and DFT solve this many-body problem. We will first start with the many-body problem, explicitly trying to find the solutions for the non-relativistic time-independent Schrödinger equation[34], as depicted in equation 2.1.

$$\mathcal{H}\left|\Phi\right\rangle = \varepsilon\left|\Phi\right\rangle \tag{2.1}$$

$$\mathcal{H} = -\sum_{i=1}^{N}\frac{1}{2}\nabla_i^2 - \sum_{A=1}^{M}\frac{1}{2M_A}\nabla_A^2 - \sum_{i=1}^{N}\sum_{A=1}^{M}\frac{Z_A}{r_{iA}} + \sum_{i=1}^{N}\sum_{j>i}^{N}\frac{1}{r_{ij}} + \sum_{A=1}^{M}\sum_{B>A}^{M}\frac{Z_A Z_B}{R_{AB}} \tag{2.2}$$

Where the Hamiltonian ($\mathcal{H}$) represents a system of nuclei and electrons which are described by two position vectors r_i and R_A, which represent the position vectors for the ith electron and the Ath nuclei[34]. The Hamiltonian represents all the kinetic and potential energy interactions between this system of N electron and M nuclei, as seen

<center>7</center>

in equation 2.2. The first term and second terms of the Hamiltonian represents the kinetic energy of the electrons and the nuclei, where M_A is the ratio of nuclei mass to that of an electron[34]. The Third term defines the Coulomb attraction between the N electrons and M nuclei, where Z_A represents the atomic number of nuclei A. The fourth and fifth terms showcase the Coulomb repulsion between each of the N electrons with each other and each of the M nuclei with each other. The units used in equation 2.2 are atomic units for simplicity.

The solution for the many-body problem is extremely difficult to solve analytically; however, it can be solved using iterative methods. Even with iterative methods, the Schrödinger equation for this problem becomes impossible to solve for large systems. This is where the Born-Oppenheimer approximation (BOA)[35] comes into play. The basis of the BOA is that since the nuclei are much more massive than electrons, we can approximate the positions of the nuclei to be fixed[34]. This allows us to view this many-body system as a system of electrons moving in the potential field of fixed nuclei. With this approximation, the kinetic energy term for the nuclei goes to zero, and the Coulomb repulsion between nuclei becomes a constant[34], which can be dropped as well. This new simplified Hamiltonian is called the electronic Hamiltonian (equation 2.3), which describes the motion of N electrons in a field of M nuclei charges.

$$\mathcal{H} = -\sum_{i=1}^{N} \frac{1}{2} \nabla_i^2 - \sum_{i=1}^{N} \sum_{A=1}^{M} \frac{Z_A}{r_{iA}} + \sum_{i=1}^{N} \sum_{j>i}^{N} \frac{1}{r_{ij}} \tag{2.3}$$

$$\varepsilon_{tot} = \varepsilon_{elec} + \sum_{A=1}^{M} \sum_{B>A}^{M} \frac{Z_A Z_B}{R_A} \tag{2.4}$$

When this Hamiltonian is applied to the Schrödinger equation (equation 2.1), the total energy from the electron-electron interactions is given; however, this is not the total energy of the system. There is still a constant factor of the nuclei-nuclei repulsion dropped from the electronic Hamiltonian. This total energy (equation 2.4)

can then be used to help solve the Hamiltonian for the nuclei-nuclei interactions[34]; thus, the BOA greatly simplifies the many-body problem. However, the BOA only considers the spatial position of the electrons while neglecting the spin[34]. In order to get the full picture of the electron-electron interactions, the effects of spin needed to be taken into consideration. This leads to the introduction of Slater determinants and the Hartree-Fock Approximation (HFA).

Before introducing Slater determinant and the HFA, the idea of a spin orbital must be discussed. The spin of a fermion is an intrinsic value that is vital in understanding the properties of electrons. To include the spin in this new formalism, an additional spin coordinate ω is added to the set of spatial coordinates $\mathbf{r}$. This new set of coordinates will be defined as $\mathbf{x}$, and is described in equation 2.5[34]. The electronic Hamiltonian given in equation 2.3 does not have any spin dependence; however, this is okay as long as our wave function has spin dependence and satisfies the *antisymmetry principle*. The *antisymetry principle* is a generalization of the Pauli exclusion principle. It states that a many-electron wave function must be antisymmetric with respect to the interchange of the coordinate $\mathbf{x}$ of any two electrons[34]. This principle is stated in equation 2.6. From this we see that the exact wave function for the many-electron system must both satisfy the Schrödinger equation and the *antisymmetry* principle. The slater determinant solves this issue by using spin orbitals.

$$\mathbf{x} = \{\mathbf{r}, \omega\} \tag{2.5}$$

$$\Phi(x_1, ..., x_i, ..., x_j, ..., x_N) = -\Phi(x_1, ..., x_j, ..., x_i, ..., x_N) \tag{2.6}$$

An orbital is a wave function that defines a single particle. A spatial orbital $(\psi_i(\mathbf{r}))$ is a function of position only and can be used to find the probability of finding an electron in an infinitesimal volume element $d\mathbf{r}$. Spatial orbitals will form

an orthonormal set, and if that set is complete, then any arbitrary function can be expanded, as shown in equation 2.7[34], where a_i are constants. In general, a set can only be complete if it is infinite, but in reality, that is an impossibility. Therefore, we will look at finite sets, where i spans from 1 to K orbitals[34]. A spin orbital ($\chi(\mathbf{x})$) is a wave function of that describes both the spatial distribution and spin of a particle. The spin orbital is defined in equation 2.8 and is a function of the spatial orbital along with two orthonormal spin functions $\alpha(\omega)$ and $\beta(\omega)$, where $\alpha(\omega))$ and $\beta(\omega)$ represent the spin-up and spin-down configurations respectively[34]. Given a set of K spatial orbitals, we can see from equation 2.8 that we will have a set of 2K spin orbitals. Additionally, since the spatial orbitals and the spin-functions are orthonormal, so will the spin orbitals.

$$f(\mathbf{r}) = \sum_{i=1}^{\infty} a_i \psi_i(\mathbf{r}) \tag{2.7}$$

$$\chi(\mathbf{r}) = \begin{cases} \psi(\mathbf{r})\alpha(\omega) \\ \quad or \\ \psi(\mathbf{r})\beta(\omega) \end{cases} \tag{2.8}$$

Now that the spin orbital has been defined for a single particle, we now consider what the wave functions will look like for a collection of particles (N electrons). Before considering the exact wave function of an interacting system of electrons, we will look at a system of non-interacting particles. In this system, the Hamiltonian will be described by equation 2.9, where the h(i) operator denotes the kinetic and potential energy of electron i[34]. An effective h(i) can also be used that includes electron-electron interaction, as long as the repulsion is denoted in some average way[34]. These h(i) operators will have a set of eigenfunctions that we take to be a set of spin orbitals (equation 2.10)[34]. From equation 2.10, the set of eigenfunctions of the Hamiltonian

$\mathcal{H}$ can be deduced. Since $\mathcal{H}$ is a sum of the operator h(i), the eigenfunction/wave function of this Hamiltonian can be described by a product of the spin orbitals for each of the electrons, as seen in equation 2.11[34]. Since Ψ^{HP} is an eigenfunction of $\mathcal{H}$, the eigenvalue E as seen in equation 2.12 can be written as the sum of the spin orbital energies of each χ_i as seen in equation 2.11[34]. This many-electron wave functionΨ^{HP} is known as the Hartree-Product (HP), and describes the wave function for non-interacting electrons, but neglects the antisymmetry principle. This is handled by the Slater determinant.

$$\mathcal{H} = \sum_{i=1}^{N} h(i) \tag{2.9}$$

$$h(i)\chi_j(\mathbf{x}_i) = \varepsilon_j \chi_j(\mathbf{x}_i) \tag{2.10}$$

$$\Psi^{HP}(x_1, x_2, ..., x_N) = \chi_i(x_1)\chi_j(x_2)...\chi_k(x_N) \tag{2.11}$$

$$\mathcal{H}\Psi^{HP} = E\Psi^{HP} \tag{2.12}$$

To modify the HP, antisymmetry needs to be satisfied. The basis for antisymmetry is that when the coordinate $\mathbf{x}$ is interchanged for two electrons, the corresponding wave functions will need to be antisymmetric. Consider a system of two electrons, where equations 2.13 and 2.14 represent the HP-wave function for electron 1 in χ_i and electron 2 in χ_j and vice-versa for equation 2.14[34]. The issue with the wave functions in equations 2.13 and 2.14 are that they distinguish between electrons, and electrons are indistinguishable. They also do not follow the *antisymmetry principle.* However, if a linear combination of the two are taken, both of these issues can be solved. This new antisymmetric wave function is detailed in equation 2.15, where C

is a normalization constant[34]. From equation 2.15 we can see that an interchange of coordinate $\mathbf{x}$ does lead to the new wave function to be antisymmetric, due to the negative sign within equation 2.15. It also satisfies the Pauli exclusion principle, since if i=j then the wave function vanishes. From here, equation 2.15 can be written in terms of a determinant, the Slater determinant (equation 2.16)[34]. Equation 2.16 can then be generalized for a system of N electrons (equation 2.17). Antisymmetrizing the HP results in the Slater determinant, which also introduces exchange effects. To be more specific, the Slater determinant incorporates exchange correlation, which means that two electrons with parallel spins will be correlated with each other while electrons with opposite spins will not[34].

$$\Psi_{1,2}^{HP}(\mathbf{x}_1, \mathbf{x}_2) = \chi_i(x_1)\chi_j(x_2) \tag{2.13}$$

$$\Psi_{2,1}^{HP}(\mathbf{x}_1, \mathbf{x}_2) = \chi_i(x_2)\chi_j(x_1) \tag{2.14}$$

$$\mathbf{\Psi} = C(\chi_i(x_1)\chi_j(x_2) - \chi_i(x_2)\chi_j(x_1)) \tag{2.15}$$

$$\mathbf{\Psi}(x_1, x_2) = C\begin{vmatrix} \chi_i(x_1) & \chi_j(x_1) \\ \chi_i(x_2) & \chi_j(x_2) \end{vmatrix} \tag{2.16}$$

$$\mathbf{\Psi}(x_1, x_2) = C\begin{vmatrix} \chi_i(x_1) & \cdots & \chi_k(x_1) \\ \vdots & \ddots & \vdots \\ \chi_i(x_N) & \cdots & \chi_k(x_N) \end{vmatrix} = |\chi_1\chi_2\cdots\chi_N\rangle \tag{2.17}$$

2.2 Hartree-Fock Approximation

The HFA has been one of the essential approximation methods for the many-electron problem since its conception. Most computational techniques in quantum chemistry

and physics use the HFA as a starting point, including DFT. The ground state wave function of an N-electron system can be described by a single slater determinant (equation 2.18)[34]. The variation principle from quantum mechanics tells us that the best possible wave function for this ground state is the one that gives us the lowest possible energy. This is stated in equation 2.19, where $\mathcal{H}$ is the electronic Hamiltonian. In equation 2.19, the variation term is the choice of spin orbital. Therefore, the minimization of E_0 is done by varying the spin orbitals[34]. In doing this minimization, the Hartree-Fock (HF) equation can be derived (equation 2.20)[34].

$$|\Psi_0\rangle = |\chi_1\chi_2...\chi_N\rangle \tag{2.18}$$

$$E_0 = \langle\Psi_0|\mathcal{H}|\Psi_0\rangle \tag{2.19}$$

$$f(i)\chi(x_i) = \varepsilon\chi(x_i) \tag{2.20}$$

Within the HF equation the operator f(i) is denoted as the Fock operator, and is an effective single-electron operator with the form described in equation 2.21. Due to the HF equation representing a single equation, equation 2.21 will look at the operator f in terms of a single electron, electron 1. In equation 25 a/b represent spin orbitals χ_a and χ_b. The operators h(i), $\mathcal{J}_b(i)$, and $\mathcal{K}_b(i)$ are described in equations 2.22-2.24, respectively[34]. The operator h(i) represents the one-electron core Hamiltonian, which is the kinetic and potential energy of a single electron with the nuclei-core. Operator $\mathcal{J}_b(i)$ is called the Coulomb operator, representing the average potential at x_i from the electron denoted by χ_b. The operator $\mathcal{K}_b(i)$ is defined as the exchange operator. The exchange operator is a non-local operator, meaning that unlike the coulomb operator, there does not exist an average potential due to $\mathcal{K}_b(i)$ at x_i. Operator $\mathcal{K}_b(i)$ acting on a spin orbital ($\chi_a(i)$) depends on the value of the orbital in all space, not just locally

13

around x_i [34]. The coulomb operator and exchange operator are sometimes denoted together as the HF-potential (equation 2.25) [34].

$$f(1) = h(1) + \sum_{b \neq a} \mathcal{J}_b(1) - \sum_{b \neq a} \mathcal{K}_b(1) \qquad (2.21)$$

$$h(1) = -\frac{1}{2}\nabla_1^2 - \sum_A \frac{Z_A}{r_{1A}} \qquad (2.22)$$

$$\mathcal{J}_b(1) = \int d\mathbf{x}_2 \chi_b^*(2) r_{12}^{-1} \chi_b(2) \qquad (2.23)$$

$$\mathcal{K}_b(1) = \int d\mathbf{x}_2 \chi_b^*(2) r_{12}^{-1} \chi_a(2) \qquad (2.24)$$

$$v^{HF}(1) = \sum_{b \neq a} \mathcal{J}_b(1) - \mathcal{K}_b(1) \qquad (2.25)$$

As seen in equations 2.21-2.25, the HF-potential is dependent on the spin orbitals of other electrons. As a result, the HF-equation is non-linear and must be solved using iterative methods. One of the procedures to solve the HF-equation is called the self-consistent field (SCF) method [34]. The SCF method starts by taking a guess of the spin orbitals and then calculating the HF-potential for each electron in the system. Then the SCF method used equation 24 to solve for a new set of spin orbitals, and thus a new HF-potential [34]. This process is repeated until self-consistency is reached, meaning that the HF-potential no longer changes. The HF-equation solution gives a set of k orthonormal spin orbitals, with orbital energies ε_k. From these k orbitals, the N orbitals with the lowest energies are defined as the occupied spin orbitals [34]. These N orbitals can be used to form a Slater determinant which can provide the HF-ground state wave function. This is the basis of the HFA, a very powerful approximation to the many-electron quantum system.

2.3 Density Functional Theory and the Kohn-Sham Equations

One of the issues with HFA is that it does not take into account the correlation energy between electrons. As a result, the HFA always overestimates the actual energy of a many-electron system; this, is where DFT comes into play. Density functional theory is a theory of correlated many-body systems[36] and is one of the most utilized computational methods of solving the many-body problem. The original theorems on DFT were published by P. Hohenberg and W. Kohn in 1964[37], but they had no idea on how to implement these theorems. In 1965, W. Kohn and L.J. Sham published a paper that provided a way to implement DFT, this paper outlines the basis of modern-day DFT[38]. The original article by Hohenberg and Kohn[37] stated that DFT was a formulation that could work with any system of interacting particles in some external potential. This includes a problem with electrons and fixed nuclei, as stated in the Hamiltonian in equation 7[36]. DFT is based on two main theorems which were proved by Hohenberg and Kohn[37]. The first theorem states for any system of interacting particles in an external potential, the external potential can be determined uniquely (apart from a constant) by the ground state particle density. The second theorem states that a universal energy functional of the particle density can be defined for a valid external potential, and that the density that minimizes the functional is the ground state density for that system[36;37]. What follows from these theorems is that all the properties of a many-body system can be determined from the ground state particle density. The energy functional alone can determine the ground state density.

From the two theorems of DFT, the issue becomes how to solve the ground state particle density in an interacting system. The approach in the Kohn-Sham paper[38] states that the ground state density for an interacting system is the same as for an auxiliary non-interacting system[36;39]. Since this auxiliary system is non-interacting, the Hamiltonian of the system can be described as in equation 2.26, where V^σ represents the effective local potential acting on an electron of spin σ at point $\mathbf{r}$[36]. This

Hamiltonian in equation 2.26 and its respective energy functional represent all the effects of a non-interacting system. All the interaction-energy contributions are then wrapped up in an exchange-correlation energy function ($E_{xc}[n]$)[36;39]. Therefore, the total Kohn-Sham energy functional can be described as in equation 2.27[36]. Where T_s represents the independent-particle kinetic energy, $E_{Hartree}$ (equation 2.28) is the Coulomb interaction of the particle density ($n(r)$) with itself, and E_{II} is the interaction energy between nuclei[36].

$$\mathcal{H}_{aux}^{\sigma} = -\frac{1}{2}\nabla^2 + V^{\sigma}(\mathbf{r}) \tag{2.26}$$

$$E_{KS}[n] = T_s[n] + \int d\mathbf{r}V_{ext}(\mathbf{r})n(\mathbf{r}) + E_{Hartree}[n] + E_{II} + E_{xc}[n] \tag{2.27}$$

$$E_{Hartree}[n] = \frac{1}{2}\int d^3r d^3r' \frac{n(\mathbf{r})n(\mathbf{r}')}{|\mathbf{r}-\mathbf{r}'|} \tag{2.28}$$

From the Kohn-sham energy function (equation 2.27), all that is needed to find the ground state particle density is to minimize this functional with respect to the particle density. To do that the exchange-correlation functional needs to be approximated. Long-range interactions are encompassed within the Hartree energy functional. Generally, the exchange-correlation functional is dependent on the local particle density[39]. This local exchange-correlation energy functional is represented in equation 2.29[36]. Where ϵ_{XC} represents the energy per electron at a point $_r$ that depends only on the particle density in the neighborhood of that point[36]. This type of exchange-correlation approximation is called local density approximation (LDA). Another approximation is called the generalized gradient approximation (GGA), and is represented in equation 2.30[36]. GGA allows for the exchange-correlation functional to depend on the gradient of the local density and is generally more accurate than LDA[36;39]. Depending on the problem at hand, there are many different types of LDA

and GGA exchange-correlation functional by various authors, each of them with a basis in either equation 2.29 or 2.30, but then altered to satisfy the needs of the specific problem.

$$E_{XC}[n] = \int d\mathbf{r} n(\mathbf{r})\epsilon_{XC}(n(\mathbf{r})) \tag{2.29}$$

$$E_{XC}^{GGA}[n] = \int d\mathbf{r} n(\mathbf{r})\epsilon_{XC}(n(\mathbf{r}), \nabla n(\mathbf{r})) \tag{2.30}$$

Solving the Kohn-Sham equation (equation 2.31) is achieved by a SCF iterative cycle, similar to the one used with HFA. This method is used to calculate the electron density of a many-body system, and then that can be used find the ground state energy of that system. The first step in the DFT-SCF cycle involves an initial guess of the electron density n(r)[36]. The effective potential (as in equation 2.26) can be calculated from the Kohn-Sham energy functional as in equation 2.32[36]. Once V^σ is calculated, the Kohn-Sham equation can be solved. The wave function from the Kohn-Sham equation can then be used to calculate a new electron density (equation 2.33). If the initial guess and the final result for the electron density are not consistent with each other to a certain degree, the process is repeated until self-consistency is achieved[36]. Once self-consistency is reached, the physical properties of the system can be calculated. For example, in a DFT geometry optimization calculation the forces acting on the system will be calculated. If these forces are not below a certain threshold, then the coordinates are slightly altered and a new SCF cycle is started.

$$[-\frac{1}{2}\nabla^2 + V^\sigma(\mathbf{r})]\psi_i^\sigma(\mathbf{r}) = \varepsilon_i^\sigma \psi_i^\sigma(\mathbf{r}) \tag{2.31}$$

$$V^\sigma(\mathbf{r}) = V_{ext}(\mathbf{r}) + \frac{\delta E_{Hartree}}{\delta n(\mathbf{r}, \sigma)} + \frac{\delta E_{XC}}{\delta n(\mathbf{r}, \sigma)} = V_{ext}(\mathbf{r}) + V_{Hartree}(\mathbf{r}) + V_{XC}^\sigma \tag{2.32}$$

$$n(\mathbf{r}) = \sum_{\sigma} \sum_{i} f_i^{\sigma} |\psi_i^{\sigma}(\mathbf{r})|^2 \tag{2.33}$$

2.4 Pseudopotentials

There are many computational packages that utilize DFT. The one used in the research covered in this paper is the Siesta program[33]. Most modern DFT programs utilize pseudopotentials in their calculations. The primary use of a pseudopotential is to replace the strong coulomb effects of the atom nuclei and core electrons with an effective ionic potential that acts on the valence electrons[36]. This can be done since an atom's core electrons and nuclei do not play a huge role in electronic structure calculations. This simplification significantly reduces the computation time in DFT calculations, and therefore is widely used. The two main types of pseudopotentials are norm-conserving and ultrasoft[36]. Here I will briefly discuss norm-conserving pseudopotentials, as they were used in all Siesta calculations. Norm-conserving pseudopotentials (NCPP) have two significant conditions, that the NCPP must equal the atomic potential outside a certain radial-cutoff value and that inside the radial cutoff value the norm of each NCPP wave function must be equal to the all-electron norm[36]. These two conditions are stated in equations 2.34 and 2.35 respectively, and the general form of a NCPP is stated in equation 2.36[36]. The all-electron wave function represents the atom without the pseudopotential approximation, and this wave function is an important reference to check against pseudopotentials. In equation 2.36, δV_l will equal zero when r is greater than the cutoff value, satisfying equation 2.34[36]. In terms of norm-conservation with equation 2.35, there is freedom in the choice of V_l. This is because there is no one perfect pseudopotential for a given element. Each pseudopotential will need to be optimized for their particular use.

$$\psi_l^{PS}(\mathbf{r}) = \psi_l^{AE}(\mathbf{r}), r > r_c \tag{2.34}$$

$$\int_0^{r_c} r^2 \left| \psi_l^{PS}(\mathbf{r}) \right|^2 d\mathbf{r} = \int_0^{r_c} r^2 \left| \psi_l^{AE}(\mathbf{r}) \right|^2 d\mathbf{r} \qquad (2.35)$$

$$V_{SL} = V_{local}(\mathbf{r}) + \sum_{lm} |Y_{lm}\rangle \, \delta V_l(\mathbf{r}) \, \langle Y_{lm}| \qquad (2.36)$$

2.5   Car-Parrinello Molecular Dynamics

Molecular dynamics is a powerful method in chemical physics used to understand the motion and kinetics of molecules and atoms. Within the DFT formalism, there is a method of running these MD simulations, and that is Car-Parrinello MD (CPMD)[40]. The basis of CPMD is that it uses the Lagrangian formalism in classical MD but describes the interaction potential using the Kohn-Sham energy functional (equation 2.27)[41]. In Newtonian mechanics, the equations of motion for a set of particles $\{R_I\}$ with interaction energy $E[\{R_I\}]$ are defined in equation 2.37[36]. Equation 2.37 is generally solved via numerical methods, one of the most common being the Verlet Algorithm (equation 2.38). The benefits of the Verlet algorithm is that the errors per time-step do not accumulate, and that energy is conserved over long simulations[36][?]. For simple problems, the interaction energy can be described by effective potentials like the Lennard-Jones potential; however, for MD on advanced materials this approach cannot be used.

$$M_I \ddot{\mathbf{R}}_I = -\frac{\partial E}{\partial \mathbf{R}_I} = \mathbf{F}_I[\{\mathbf{R}_J\}] \qquad (2.37)$$

$$\mathbf{R}_I(t + \delta t) = 2\mathbf{R}_I(t) + \mathbf{R}_I(t - \delta t) + \frac{(\delta t)^2}{M_i} \mathbf{F}_I[\{\mathbf{R}_J(t)\}] \qquad (2.38)$$

There have been other first-principles or quantum molecular dynamics (QMD) methods done before CPMD, the most well-known being Born-Oppenheimer MD (BOMD). One of the early advantages of BOMD was that it untangled the motion of

electrons and nuclei[41]. In BOMD, each time one of the nuclei was displaced from its original position, a new optimization of the electronic structure was calculated. Although effective, this method was computationally taxing requiring the Kohn-Sham equation to be solved for each time step[41]. In CPMD, the electrons and the nuclei evolve simultaneously. The way this is done is by treating the energy of the total system as a function of classical coordinates $\{R_I\}$ for the nuclei and quantum coordinates $\{\psi_i\}$ for the electrons[36]. CPMD is a DFT-MD method, as it uses the Kohn-Sham energy as the potential energy of the system. The total Lagrangian for CPMD is denoted in equation 2.39[36], and the first term on the RHS of the equation represents a fictitious kinetic energy for the electrons. This term is fictitious since what is truly represents is the update of the wave functions during the calculation[41]. The term $E[\psi_i, R_I]$ represents the Kohn-Sham energy functional. The last term defines the orthonormality constraint for the electronic wave functions, with Λ_{ij} as Lagrange multipliers for that constraint[36].

$$\mathcal{L} = \frac{1}{2}[\sum_{i=1}^{N}(2\mu)\int d\mathbf{r}\left|\dot{\psi}_i(\mathbf{r})\right|^2 + \sum_{I} M_I \dot{\mathbf{R}}_I^2] - E[\psi_i, \mathbf{R}_I] + \sum_{ij}\Lambda_{ij}[\int d\mathbf{r}\psi_i^*(\mathbf{r})\psi_j(\mathbf{r}) - \delta_{ij}]$$

(2.39)

Solving the Lagrangian in equation 2.39 with generalized coordinates $\{\psi_i, R_I\}$, the equations of motion for CPMD can be found (equations 2.40 and 2.41). In equation 2.41, the variation of the Kohn-Sham energy functional with respect to the wave functions is the same as solving the Kohn-Sham equation. Therefore, we can simplify equation 2.41 using the Hamiltonian. In these equations of motion, the mass of the nuclei is physical while the mass of the electrons (μ) is fictitious and can be optimized for a specific problem[36]. From equations 2.40 and 2.41 the Verlet algorithm can be applied (equations 2.42 and 2.43), where the constraint conditions (Λ_{ij}) are solved at each step so that the electron wave function is orthonormal throughout the MD

simulation[36]. The method of CPMD is a very powerful DFT-MD formulism that has been used effectively in many DFT programs, and was essential in all the calculations done in all the MD simulations done in this paper.

$$M_I \ddot{\mathbf{R}}_I = -\frac{\partial E}{\partial \mathbf{R}_I} \tag{2.40}$$

$$\mu \ddot{\psi}_i(\mathbf{r}, t) = -\frac{\delta E}{\delta \psi_i^*(\mathbf{r})} + \sum_k \Lambda_{ij} \psi_k(\mathbf{r}, t) = \mathcal{H} \psi_i(\mathbf{r}, t) + \sum_k \Lambda_{ij} \psi_k(\mathbf{r}, t) \tag{2.41}$$

$$\mathbf{R}_I^{n+1} = 2\mathbf{R}_I^{n+1} - \mathbf{R}_I^{n-1} + \frac{(\delta t^2)}{M_I} \mathbf{F}_I \tag{2.42}$$

$$\psi_i^{n+1}(\mathbf{r}) = 2\psi_i^n(\mathbf{r}) - \psi_i^{n-1}(\mathbf{r}) - \frac{(\delta t^2)}{\mu}[\mathcal{H}\psi_i^n(\mathbf{r}) - \sum_k \Lambda_{ij} \psi_k(\mathbf{r}, t)] \tag{2.43}$$

2.6   Computational Methodology

All density functional theory (DFT) and MD calculations were carried out with the Siesta package[33] utilizing relativistic norm-conserving Troullier-Martins[42] pseudopotentials, with the VdW-DF correlation[43] and the C09 exchange functional[44] (C09-VdW-DF). These pseudopotentials were generated using the ATOM program[45].

To understand the adsorption properties of the molecules used in this study, we first looked at the disassociation energy of their bonds. The molecules investigated were H2, H2O, O2, CO, CO2, and CH4. Multiple single-point calculations were done via Siesta with the C09-VdW-DF pseudopotentials with one atom in the molecule being displaced from its equilibrium position, with all the other atoms being held fixed. The disassociation energy was obtained from these single-point calculations with equation 2.44, where E_{tot} is the total energy of the system, E_{atom} is the energy

21

of the atom that is being pulled away, and E$_{\text{fixed}}$ is the energy of the partial molecule that is fixed in place.

$$E_{dis} = E_{tot} - (E_{fixed} + E_{atoms}) \tag{2.44}$$

All initial DFT relaxations were done on 2x4x2 super-cells of ZnO, with the addition of a hydrogen termination layer which was fixed in position along with the next lowest layer of ZnO. This was done to simulate the bulk properties of the ZnO surfaces, as well as preserve the coordination number of the bottom layer of ZnO atoms. To reduce interactions between repeated slabs, a 20 Åvacuum layer was introduced along the z-direction. The conjugate gradient (CG) relaxations were done with a plane wave cutoff of 200 Ry, force convergence threshold of 0.02 eV/ Å, and a 2-dimensional 8x8 k-point grid. The final xyz coordinates of the ZnO slabs after relaxation were used for all the MD simulations and calculations of the electrostatic potential.

To gain a better understanding of the relaxed surfaces, which part of the slab the molecules will interact with, the electrostatic potential of each ZnO slab was calculated. The third-party Siesta package Contour[33] was used to determine the electrostatic potential for each of the ZnO surfaces. The electrostatic potential at the surface of each slab was calculated and the potential of various points within the top layer of ZnO. For the grove/terrace defect slabs, the electrostatic potential was taken at both the uppermost surface of the slab, and at the surface of the defect.

All MD calculations were done with a Nose mass of 1500 Ry*fs^2, a target temperature of 300 K, and a 2x2 k-point grid. A time resolution of 1fs was used, and each system was allowed to evolve for a total of 20ps. The molecules used in these MD computations are the same as in the disassociation energy calculations discussed above. The pressure, temperature, and total energy of the systems were plotted over the 20ps time range, as well as the molecules' geometric position relative to the surface

of the ZnO slab and with the other atoms in the molecule.

CHAPTER III

ZnO Surfaces

3.1 Structure of ZnO Slabs

The two ZnO surfaces used in all the calculations are described by the $(10\bar{1}0)$ and $(11\bar{2}0)$ Miller indices. ZnO has a hexagonal wurtzite structure with unit vectors a and c as 3.25Å and 5.206Å respectively[28]. These type of crystal structures can be described as alternating planes of zinc and oxygen atoms stacked along the c-axis[28]. The $(10\bar{1}0)$ and $(11\bar{2}0)$ surfaces are two different cuts of the hexagonal wurtzite crystal structure, these cuts create slabs of ZnO that are perpendicular to the c-axis. The calculations were done in surfaces that are pristine, contain a dimer-defect, or slabs with edge-defects. The edge surface defects of each slab were either in the (0001) or $(10\bar{1}0)$ and $(11\bar{2}0)$ directions. The eight non-polar ZnO surfaces are listed in table 3.1 along with the corresponding identifier that will be used throughout this paper. Surface geometries of each of the slabs are shown in figures 3.1-3.8, where lower layers of the ZnO are semi-transparent.

Slab	Identifier
$10\bar{1}0$ Dimer Defect	S1
$10\bar{1}0$ Pristine	S2
$11\bar{2}0$ Dimer Defect	S3
$11\bar{2}0$ Pristine	S4
$10\bar{1}0$-Edge-0001	S5
$10\bar{1}0$-Edge-$1\bar{1}00$	S6
$11\bar{2}0$-Edge-0001	S7
$11\bar{2}0$-Edge-$\bar{1}2\bar{1}0$	S8

Table 3.1: Table states the coding used to describe the 8 ZnO surfaces used
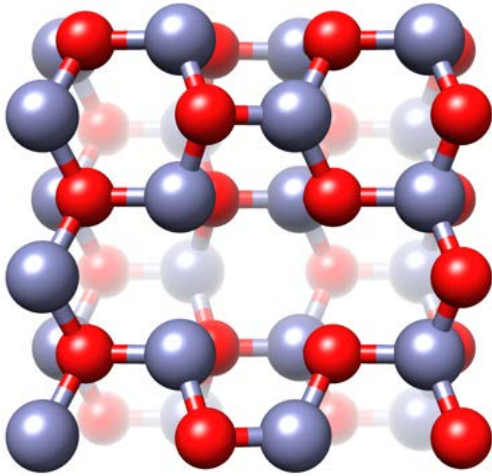
Figure 3.1: $10\bar{1}0$ surface with dimer-defect (S1)
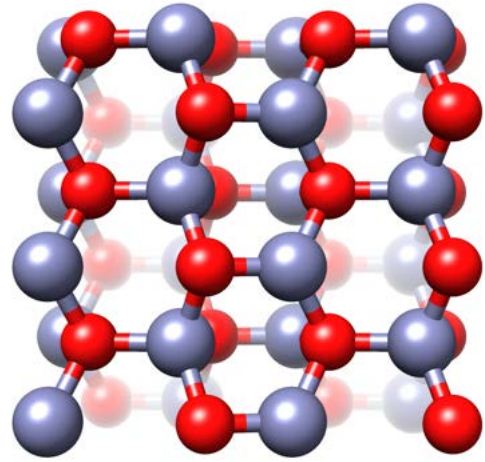
Figure 3.2: Pristine $10\bar{1}0$ surface (S2)
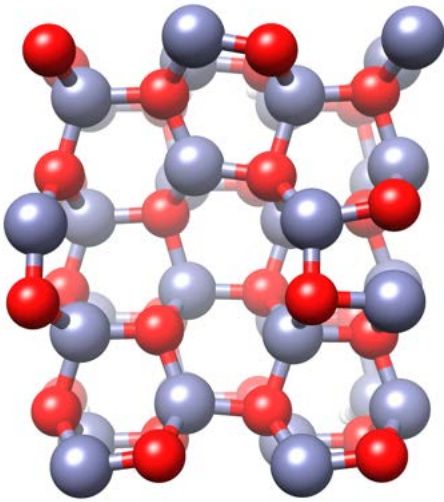
Figure 3.3: $11\bar{2}0$ surface with dimer-defect (S3)
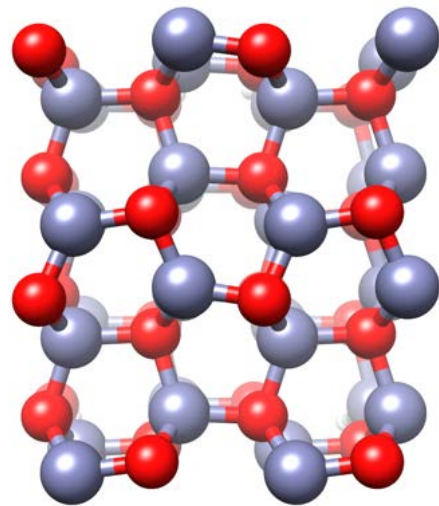
Figure 3.4: Pristine $11\bar{2}0$ surface (S4)
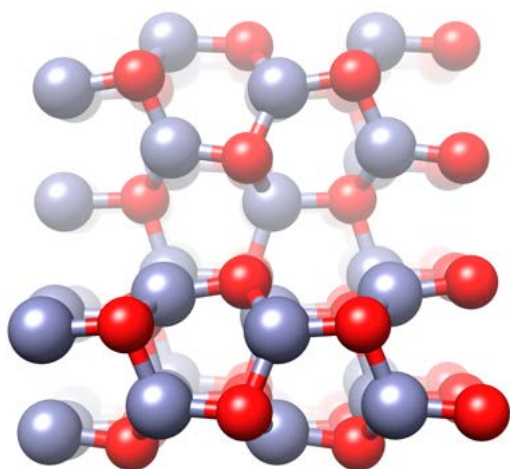
Figure 3.5: $10\bar{1}0$ surface with Edge-0001 defect (S5)
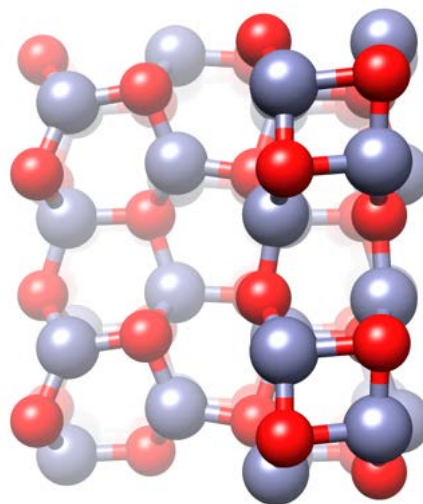
Figure 3.6: $10\bar{1}0$ surface with Edge-$1\bar{1}00$ defect (S6)
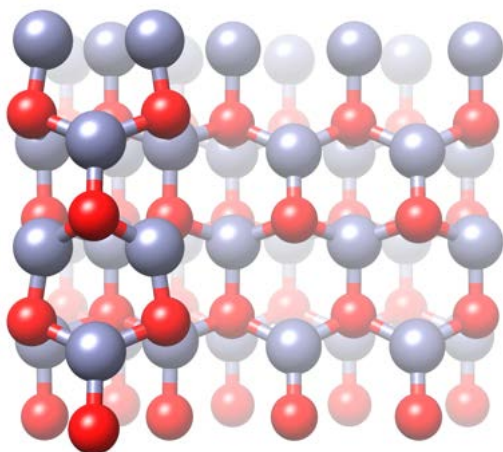
Figure 3.7: $11\bar{2}0$ surface with Edge-0001 defect (S7)
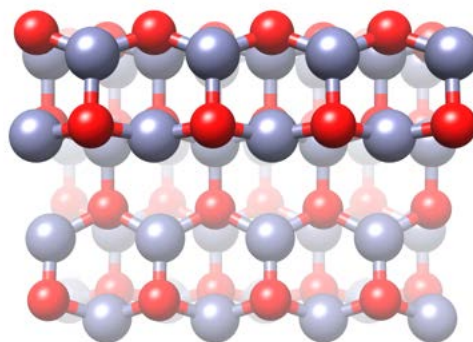
Figure 3.8: $11\bar{2}0$ surface with Edge-$\bar{1}2\bar{1}0$ defect (S8)

3.2 Electrostatic Potentials

The electrostatic potential of the slabs is critical in understanding the dynamics of molecules approaching them. The electrostatic potential on/near the surfaces of ZnO shapes how the molecules will move in and interact. The electrostatic Coulomb force is directly proportional to the gradient of the electrostatic potential. Therefore,

26

wherever the gradient of the potential is highest, it is where the molecule's bonds are more likely to break. This process is the most important for assesing catalytic activity. Figures 3.1-3.8 represent the electrostatic potential near the surface of the ZnO slabs. These contour plots show the potential in the x-y plane for each ZnO surface, with a fixed origin and spanning vectors per slab. Appendix D, table D.1 specifies the exact origin point and spanning vectors per slab. Appendix D also showcases the electrostatic potential at various planes within the surface of the ZnO slab. The dotted line in the electrostatic potential plots represents the contours of zero potential, as to help distinguish areas of high potential gradients. The points of interest in these electrostatic potential plots are near the Zn-O dimer defect and edge defects, where bond splitting is more likely to occur.

The effect of a Zn-O dimer defect is clearly presented in figures 3.1-3.4. The $(11\bar{2}0)$ defect surface (figure 3.1) shows a larger potential gradient at the defect than at any other point on the slab. Whereas in the pristine $(11\bar{2}0)$ surface the potential gradient is generally uniform throughout. This effect can also be seen to a certain extent with other surfaces, though it is much more subtle. These potential catalytic points will be of great interest in the MD calculations, especially with polar molecules like CO, H_2O, and CH_3Cl, as polar molecules will be more likely to interact with areas with high potential gradients. The edge defect surfaces (figures 3.5-3.8) provide a drastically different potential surface compared to the pristine and dimer-defect slabs. An edge defect results in a "trench" in the surface of the material, large areas of near zero potential are seen where the "trench" begins. Here the most significant catalytic effects are predicted to take place along the edge, as that is where the potential gradient is highest.
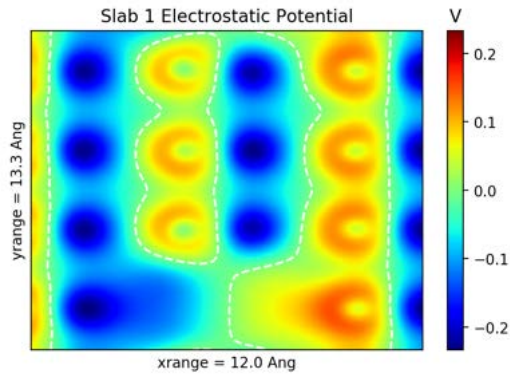
Figure 3.9: Electrostatic Potential for$10\bar{1}0$ surface (S1)
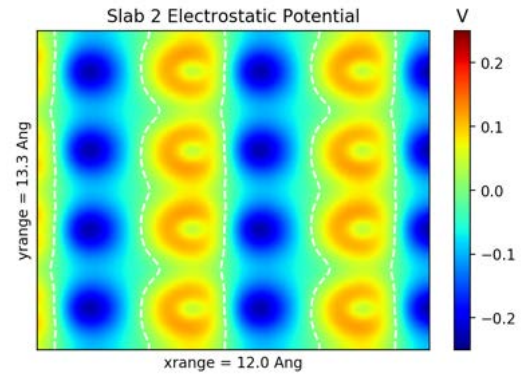
Figure 3.10: Electrostatic Potential for Pristine $10\bar{1}0$ surface (S2)
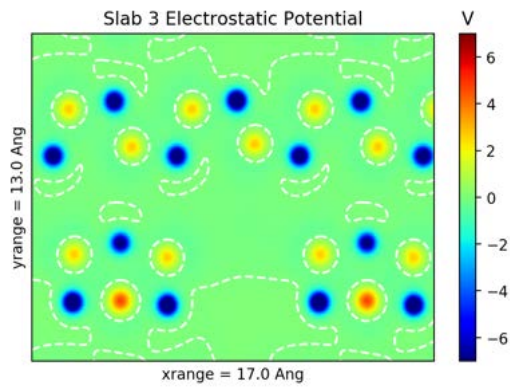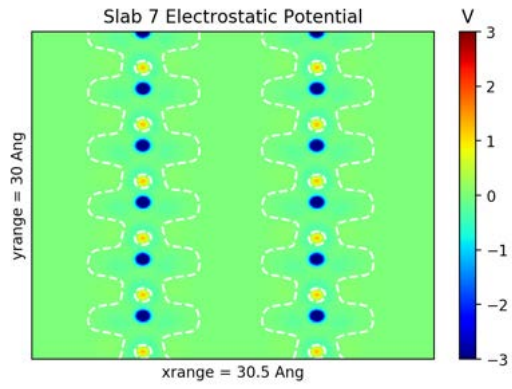

Figure 3.11: Electrostatic Potential for $11\bar{2}0$ surface with dimer-defect (S3)
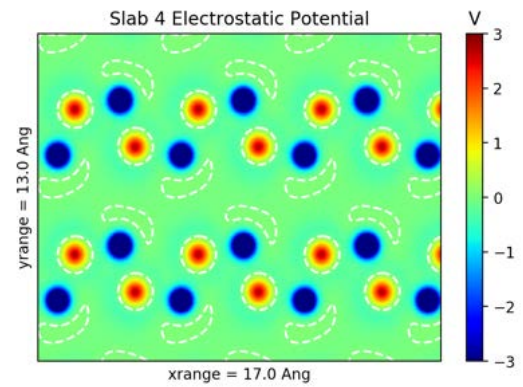
Figure 3.12: Electrostatic Potential for Pristine $11\bar{2}0$ surface (S4)
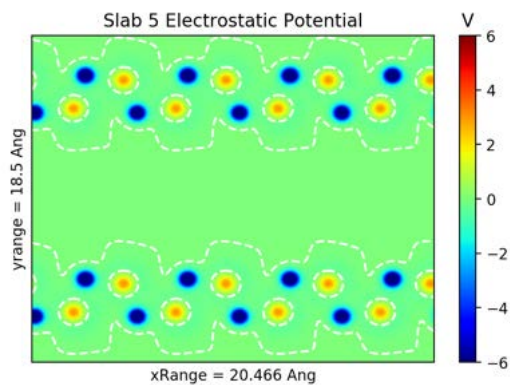
Figure 3.13: Electrostatic Potential for $10\bar{1}0$ surface with Edge-0001 defect (S5)
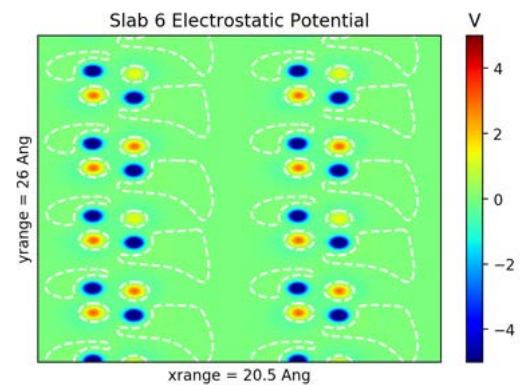
Figure 3.14: Electrostatic Potential for $10\bar{1}0$ surface with Edge-$1\bar{1}00$ defect (S6)

Figure 3.15: Electrostatic Potential for $11\bar{2}0$ surface with Edge-0001 defect (S7)
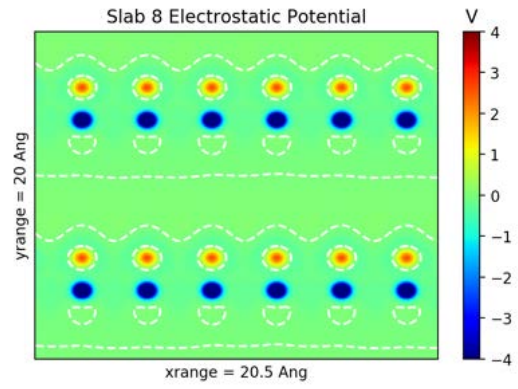
Figure 3.16: Electrostatic Potential for $11\bar{2}0$ surface with Edge-$\bar{1}2\bar{1}0$ defect (S8)

CHAPTER IV

Molecular Dynamics

4.1 Dissasociation Energy of Molecules

The FTS process is based on building hydrocarbons and alcohols from various syngas molecules near the surface of a catalytic material[2;3]. In order for these processes to happen (equations 1.1-1.4), the bonds of the molecules need to be broken. Therefore, the interaction energy of a molecule and a catalytic site needs to be sufficient enough to overcome the binding energy of the molecule. To understand the binding energy of these molecules, disassociation energy with respect to bond length plots were created. For diatomic molecules like H_2, O_2, and CO, the disassociation energy was calculated by increasing the separation length between the two atoms and calculating the binding energy at each step. For H_2O and CO_2, a single hydrogen and oxygen atom were separated from the molecule respectively, hence calculating the disassociation of a hydrogen from H_2O and an oxygen from CO_2. For CH_4 and CH_3Cl disassociation calculations, a single hydrogen and the chlorine atom were separated from CH_4 and CH_3Cl respectively. For H_2, O_2, CO, H_2O, and CO_2 plots single-point calculations were utilized via siesta, to avoid the separation distance between the atoms to change. For CH_4 and CH_3Cl, geometry optimization calculations were used instead. The reason geometry optimization calculations were used for these two molecules was to allow the hydrogen atoms in the molecule to find their optimum geometry while probing the bond energy between two specific atoms (C-H and C-Cl). Figures 4.1-4.7 represent the disassociation plots with the calculated binding energy. The binding energies ranged from -5.14 eV to -14.17 eV, with CH_3Cl having the lowest binding

energy and CO having the highest. Here these plots are used in reference with the geometric and thermodynamic results of the CPMD simulations, where if adsorption of the molecule with ZnO occurs then the amount of energy supplied to the molecule can be estimated.
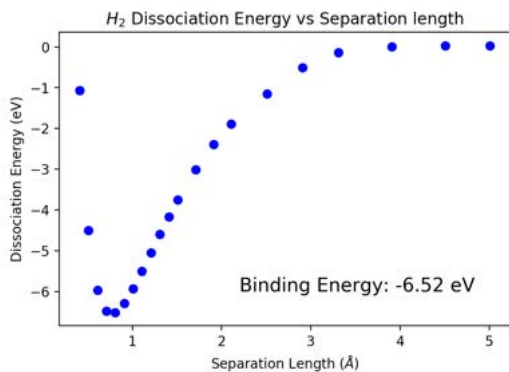
Figure 4.1: Dissasociation energy for H_2 molecule
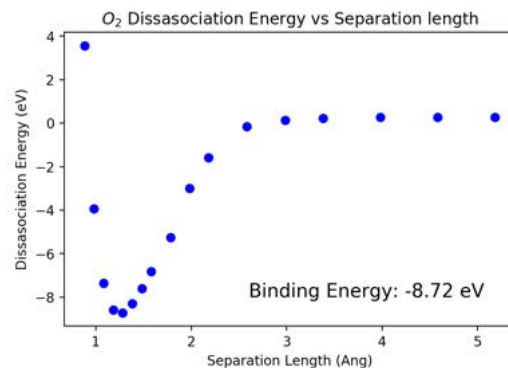
Figure 4.2: Dissasociation energy for O_2 molecule
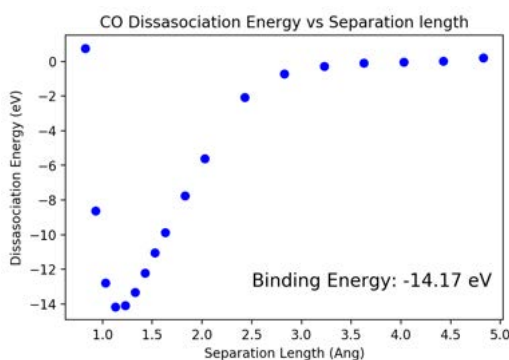
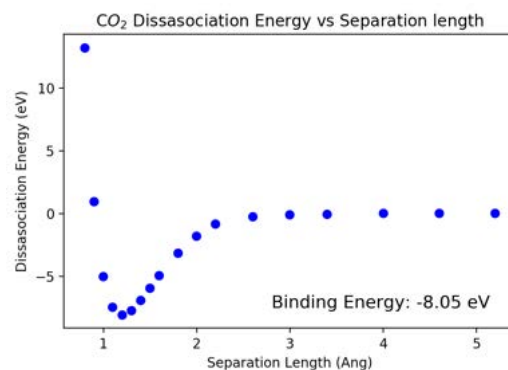Figure 4.3: Dissasociation energy for CO molecule
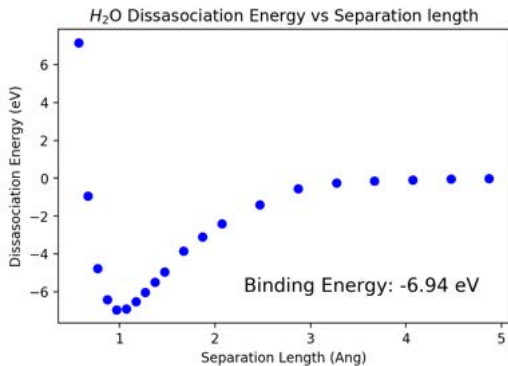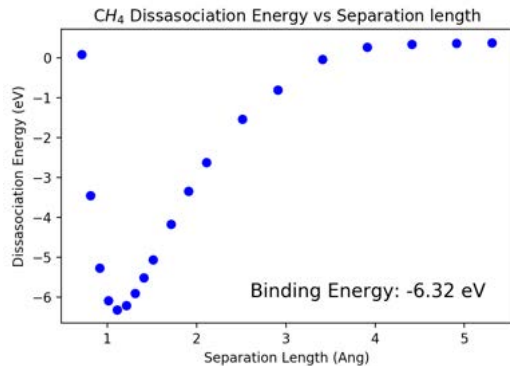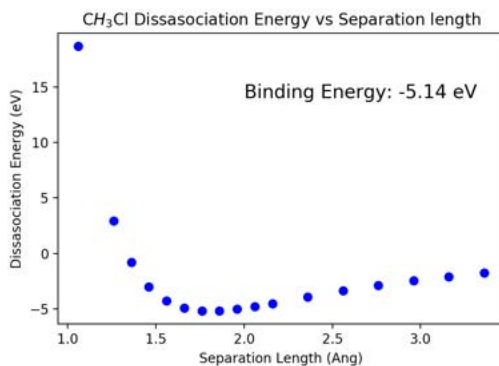

Figure 4.4: Dissasociation energy for CO_2 molecule

Figure 4.5: Dissasociation energy for H_2O molecule

Figure 4.6: Dissasociation energy for H_2O molecule

Figure 4.7: Dissasociation energy for CH_3Cl molecule

4.2 CPMD Simulations

The following sub-sections cover the most promising results of the CPMD simulations done over the eight ZnO surfaces used. These results show adsorption and/or bond-breaking within the molecules used in this study. In general, we are looking for evidence that any or all of these surfaces can be used as a catalyst in FTS. To be a viable catalyst in FTS, one of the four main reactions covered in the introduction (equations 1.1-1.4) need to occur over ZnO. The molecules used in these four reactions are H_2, CO, H_2O, and various hydrocarbons. If we see adsorption or bond-breaking within these types of molecules, that shows that there is promise for ZnO to be used as an FTS catalyst. Molecules not explicitly covered in the FTS reactions (CH_3Cl,

CO_2, and O_2) were tested to probe the adsorption effects of the ZnO surfaces, in order to better understand how ZnO interacts with a variety of molecules. The full results, including those that show no catalytic promise, can be found in Appendix E.

4.2.1 Dimer-Defect Surfaces

This section covers the CPMD simulations over the $10\bar{1}0$ and $11\bar{2}0$ surfaces. In particular, the dimer-defect surfaces of $10\bar{1}0$ and $11\bar{2}0$ ZnO.

4.2.1.1 $10\bar{1}0$ Surface

As seen in Chapter 3, the $10\bar{1}0$ dimer-defect surface (S1) has the most prominent electrostatic potential gradient. We see the greatest potential gradient above the defect-point, so it is assumed this dimer-defect would show ample catalytic activity in our CPMD simulations. This is shown in figures 4.8-4.15, with H_2, O_2, CO, and CO_2. In figure 4.8 we see that the surface S1 breaks and adsorbs the H2 molecule within 10ps. Figure 4.9 presents snapshots of when the H_2 molecules was adsorbed into the dimer-defect and when the H-H bonds break apart. This result is very promising, as the splitting of H_2 is a vital step in FTS.
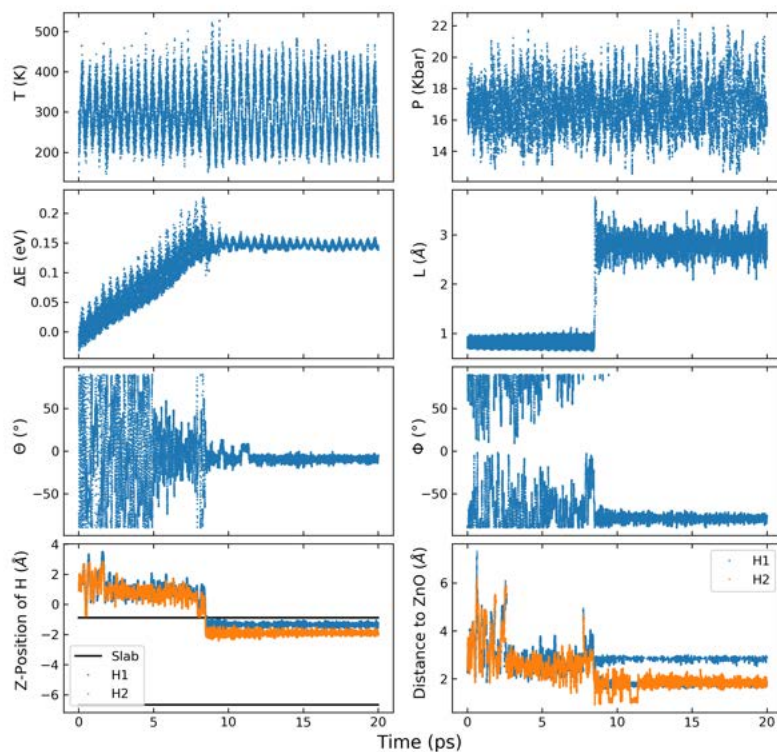
Figure 4.8: MD results for S1 with H_2

(a) t = 8.4ps

(b) t = 8.49ps
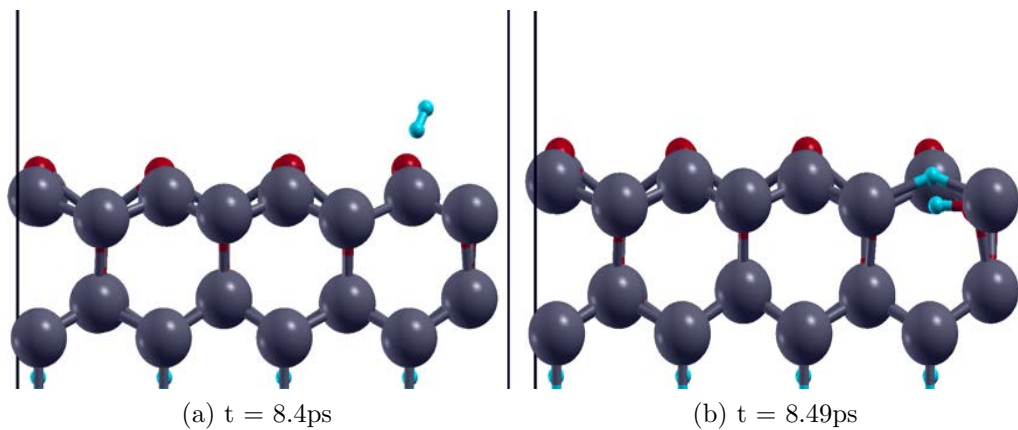
Figure 4.9: H_2 breaking its bond at dimer-defect on surface S1

However, bond-breaking was not explicitly found in the other molecules tested. For O_2 and CO_2 (figures 4.10-4.11 and 4.14-4.15) we see that the molecules were adsorbed into the dimer-defect, but their respective bonds did not break. This adsorption effect is still note-worthy, as this interaction fixed the molecules to the defect site

for the remainder of the simulation. The CO simulation (figures 4.12-4.13) is unique in that the molecule interacted weakly with the surface nearly from the start of the simulation, and it did not travel far from its original position. We also see that the azimuthal angle of the CO molecule was on average constant, while the polar angle oscillated greatly. This result will be studied in more detail in the near future, as this weak interaction with the surface (regardless of if there was a defect or not) is seen in some of our other simulations.
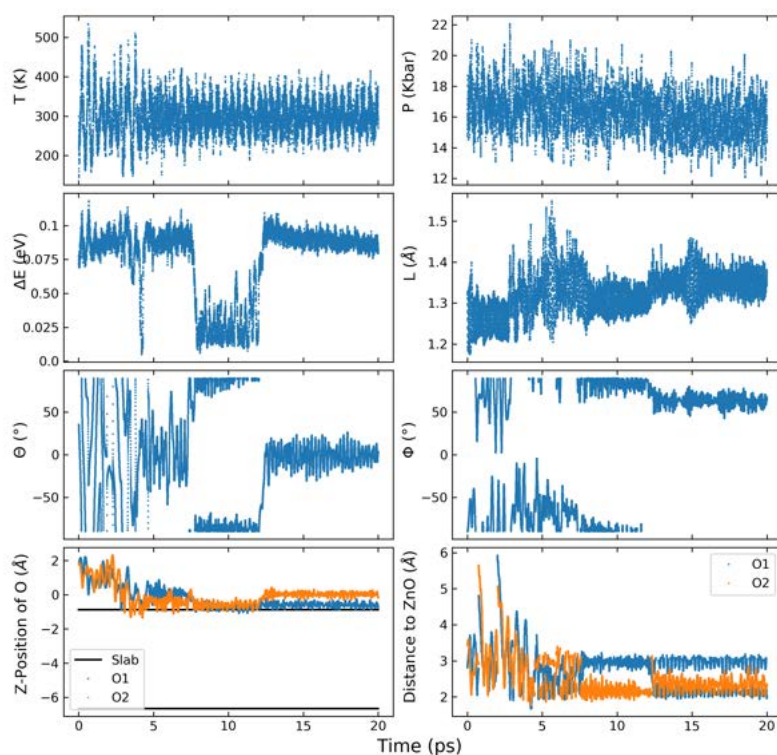
Figure 4.10: MD results for S1 with O_2
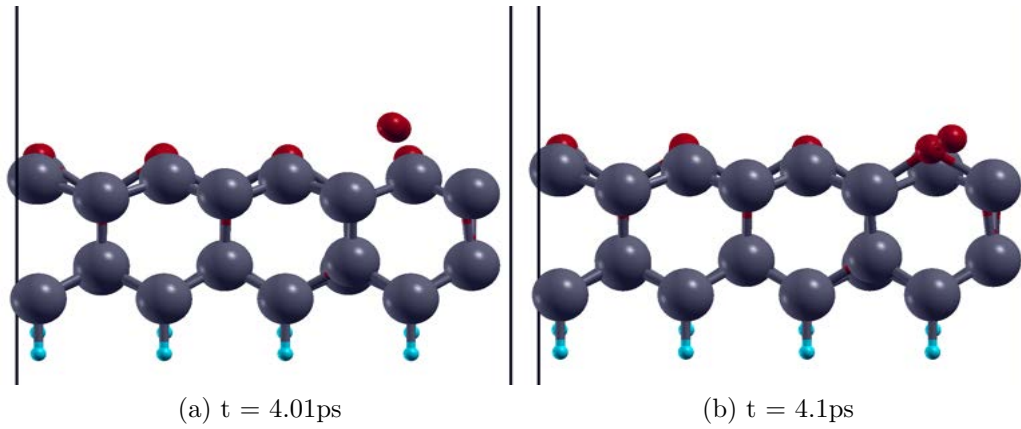
(a) t = 4.01ps   (b) t = 4.1ps

Figure 4.11: O_2 adsorbs to dimer-defect on surface S1
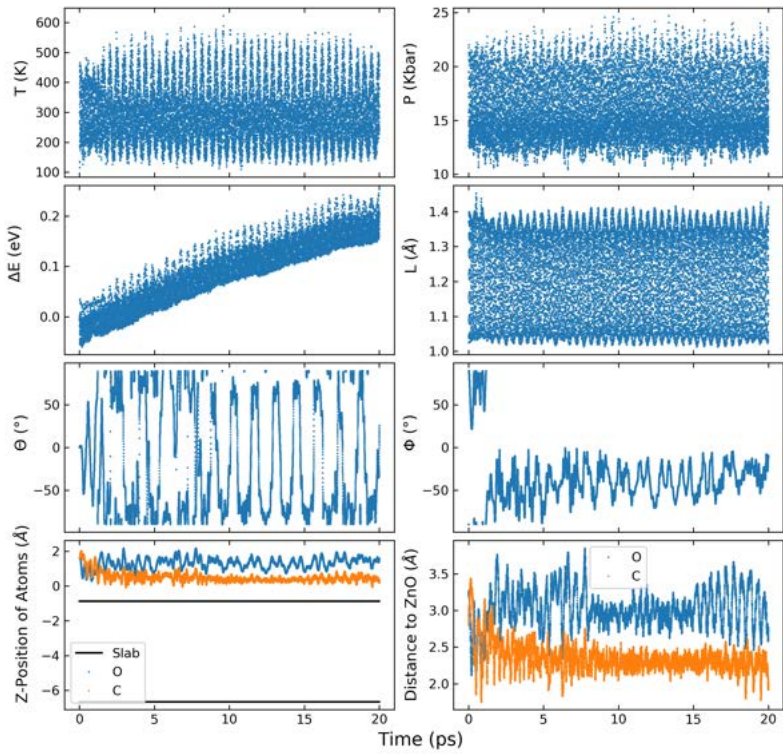
Figure 4.12: MD results for S1 with CO

(a) t = 0.0ps   (b) t = 6.91ps
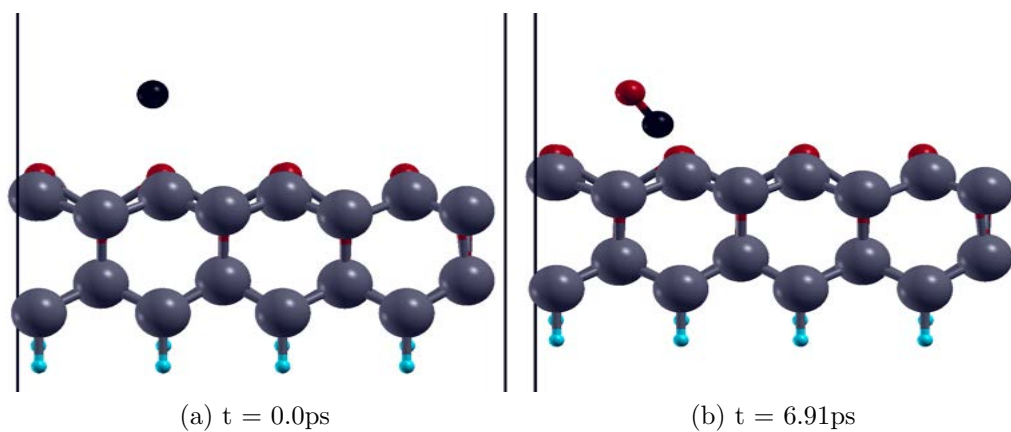
Figure 4.13: CO weak interaction with Surface S1
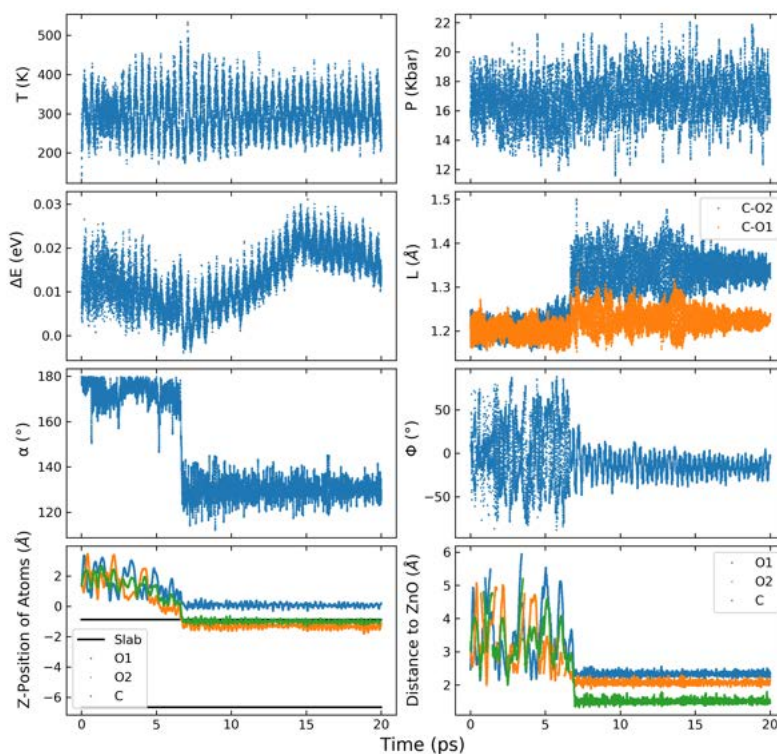
Figure 4.14: MD results for S1 with CO_2

(a) t = 6.51ps   (b) t = 7.26ps
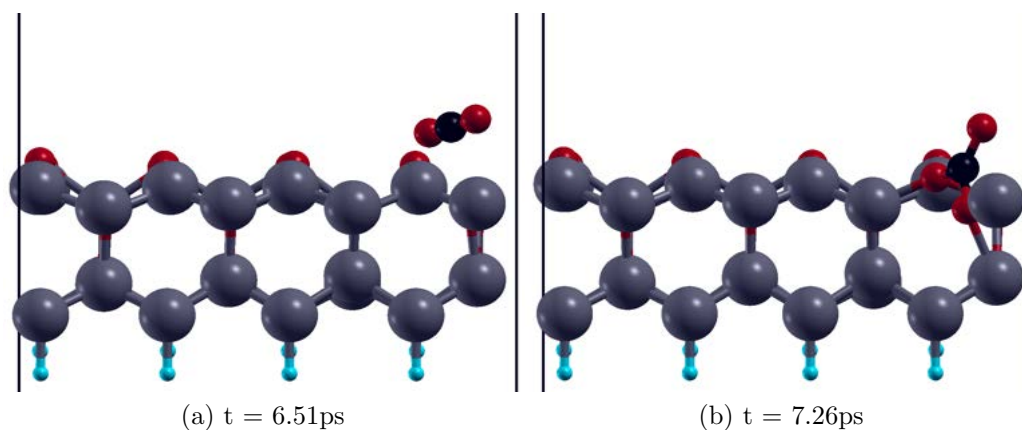
Figure 4.15: CO_2 adsorbs to dimer-defect of Surface S1

4.2.1.2 $11\bar{2}0$ Surface

Due to the calculated electrostatic potential, the $11\bar{2}0$ dimer-defect surface (S3) also showed promise with catalytic activity. The CPMD simulations for S3 showed a similar result as S1 in the case of H_2. From figures 4.16-4.17, we see that the S3 surface interaction with H_2 broke its bond and adsorbed the molecule within the defect site, again within 10ps. From this and the previous result we can verify that these dimer-defects are able to split H_2. These results also show that the dimer-defects also cause weak-interactions between various other molecules, in the case of S3, this can be seen with O_2 (figures 4.18-4.19). Here we see that the O_2 molecule was attracted to the defect-site and then subsequently stayed fixed around the defect for the rest of the simulation.
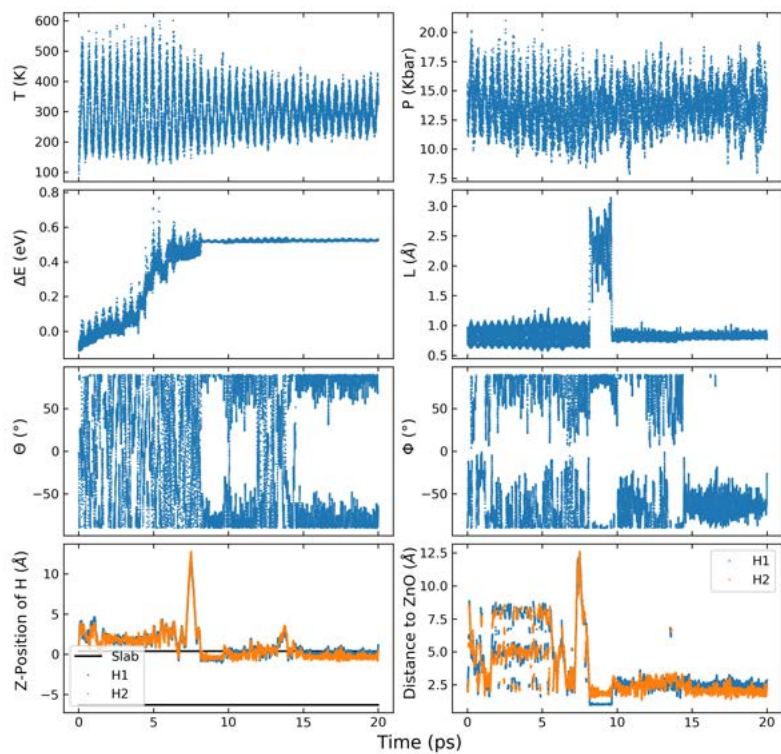
Figure 4.16: MD results for S3 with H_2

(a) t = 8.15ps

(b) t = 8.2ps
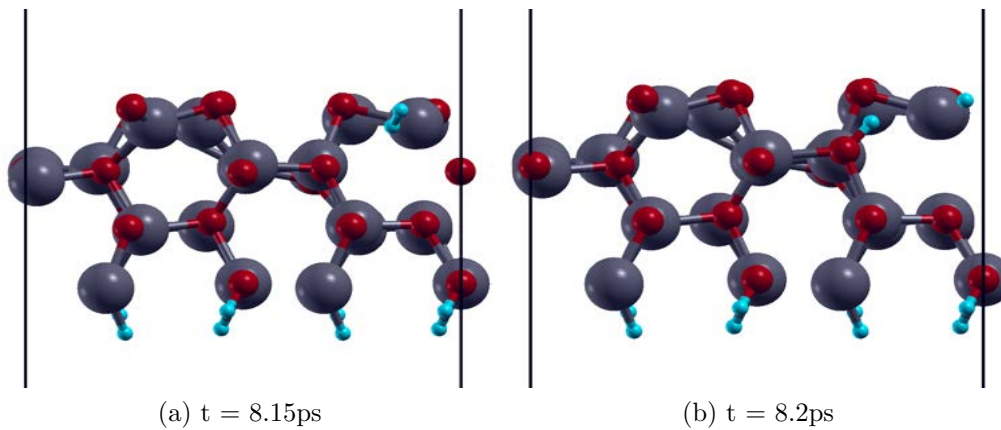
Figure 4.17: H_2 breaking its bond at dimer-defect of Surface S3
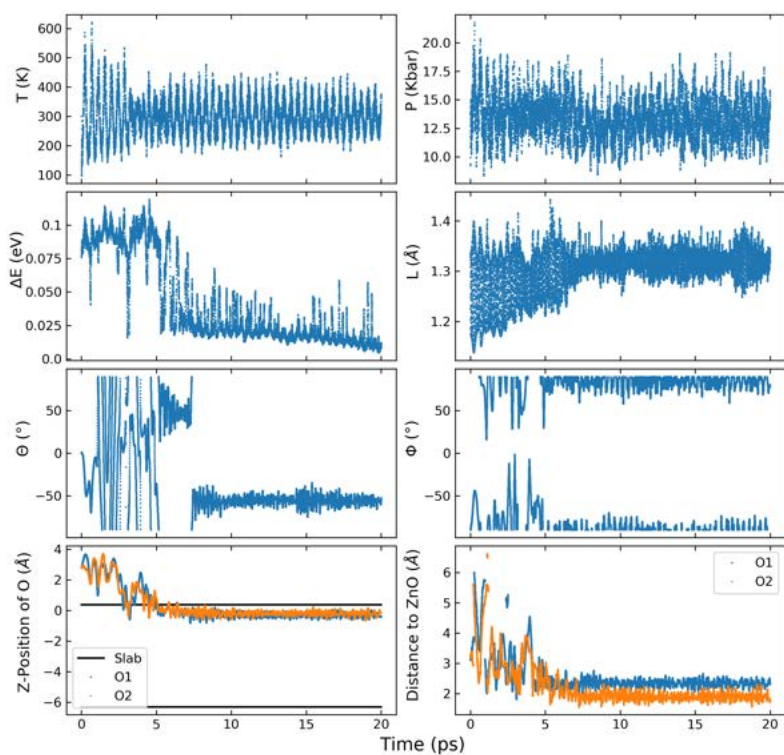
Figure 4.18: MD results for S3 with O_2
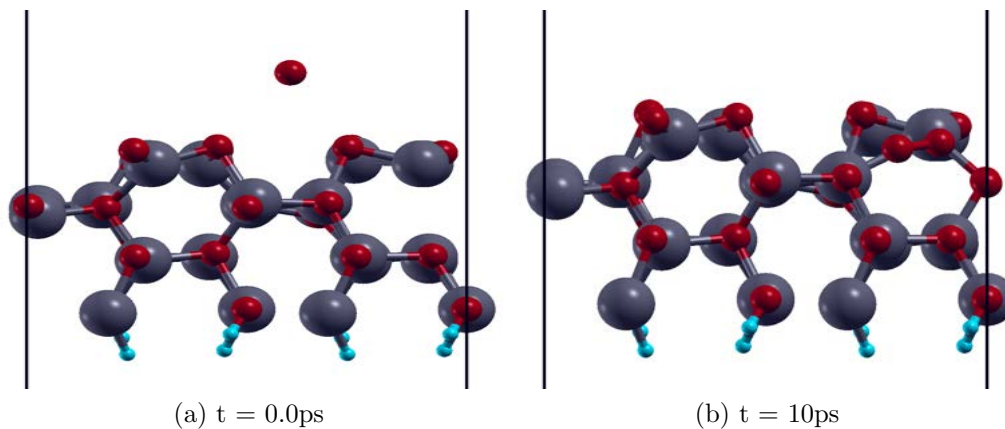

(a) t = 0.0ps

(b) t = 10ps

Figure 4.19: O_2 weak interaction with Surface S3

4.2.2 Edge-Defects

This section cover the results from the CPMD simulations of the edge-defects surfaces. The surfaces covered here are the $10\bar{1}0$ and $11\bar{2}0$ edge-defects (S5-S8), the $11\bar{2}0$-0001 edge-defect surface (S7) was omitted from this section as the data did not show

significant results, only CO weak interactions (appendix E). As seen in figures 3.5-3.8, these edge-defect surfaces are drastically different from the dimer-defect surfaces. Along with the differences in electrostatic potential, the edge-defect surfaces create a physical trench which provides an additional physical barrier for the molecules which is not found in with surfaces S1-S4.

4.2.2.1 $10\bar{1}0$-Edge-0001 Surface

For the $10\bar{1}0$-Edge-0001 Surface (S5), there were a few significant results that pertain to the FTS process. The most prominent being that CO_2 adsorbed into the interface between the edge and the top of S5. The bond between the carbon and the oxygen did not break, but the adsorption itself is significant as this was seen in with the dimer-defect surfaces as well. With this result seen in both edge and dimer-defect surfaces, additional research on this interaction could be worthwhile. Observing the interactions betwen the surface, CO_2, and another molecule like H_2 would be the next step to take, to see if more catalytic activity can be observed. In addition to CO_2, O_2 was observed to have weak interactions with the S5 edge. As with O_2 in S3, there was no clear evidence of adsorption, but the interaction with the S5 surface fixed the position and stabilized the oscillations of O_2.
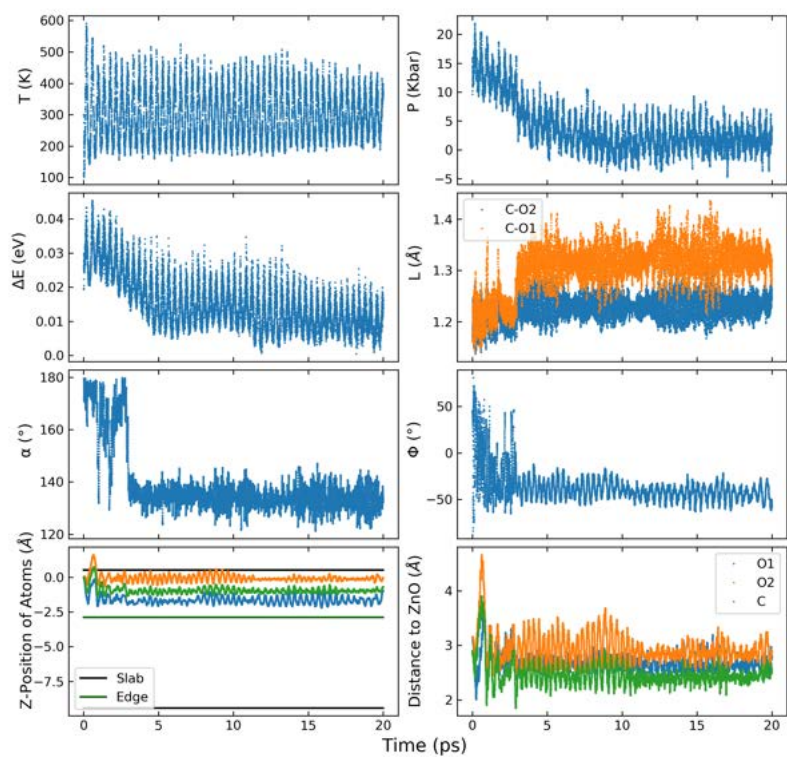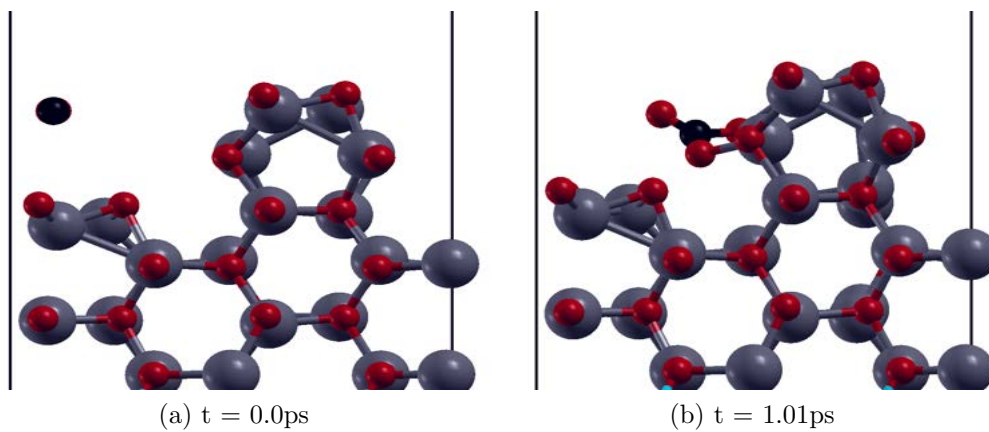
Figure 4.20: MD results for S5 with CO2

(a) t = 0.0ps

(b) t = 1.01ps

Figure 4.21: CO2 adsorbs surface of Surface S5
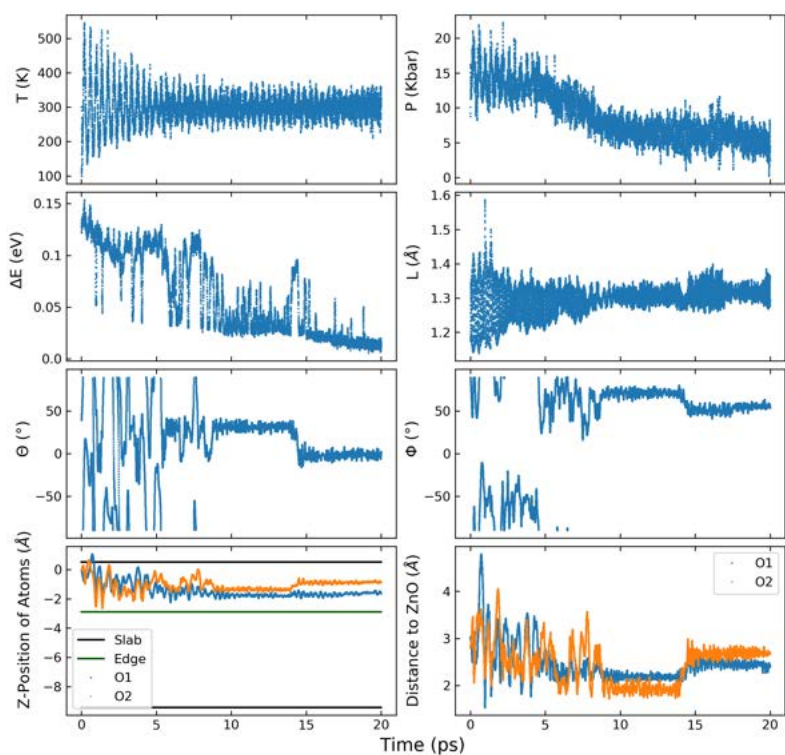
Figure 4.22: MD results for S5 with O_2

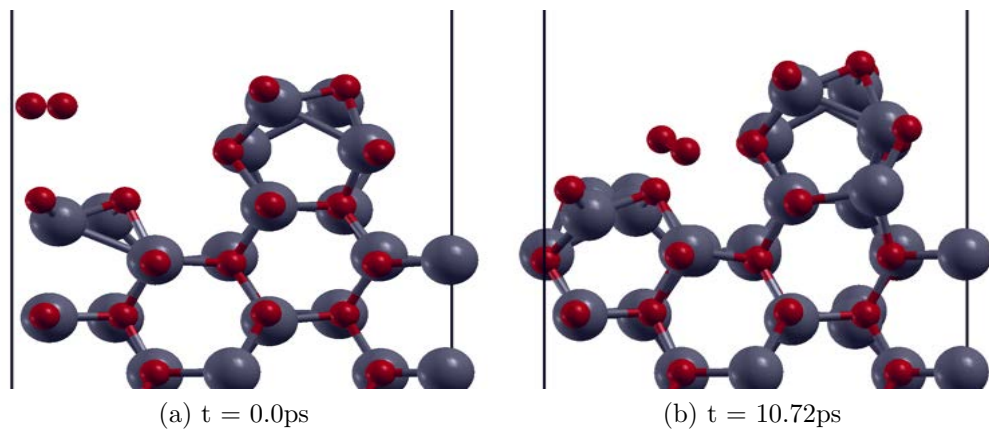(a) t = 0.0ps

(b) t = 10.72ps

Figure 4.23: O_2 weak interaction with Surface S5

4.2.2.2 $10\bar{1}0$-Edge-$1\bar{1}00$ Surface

The $10\bar{1}0$-Edge-$1\bar{1}00$ Surface (S6) results showed promise in regards to H_2 and H_2O (figures 4.24-4.27). Near the walls of the edge-defect, the bond of H_2 and H_2O were

broken. In regards to H_2 (figures 4.24-4.25), the edge-defect split the molecule between the wall of the defect and the surface of the edge within 5ps. This resulted in one of the largest separation lengths (distance between H atoms in H_2) of any other the runs. H2O provided similar results, where the bond between OH-H was split near the walls of the edge-defect. This result is significant because S6 is the only ZnO defect/surface combination with the ability to split water molecules. There have been studies on doped/hybrid ZnO crystals and materials that can split water, but not for non-polar ZnO $10\bar{1}0$ and $11\bar{2}0$ defect-surfaces[46;47;48;49].
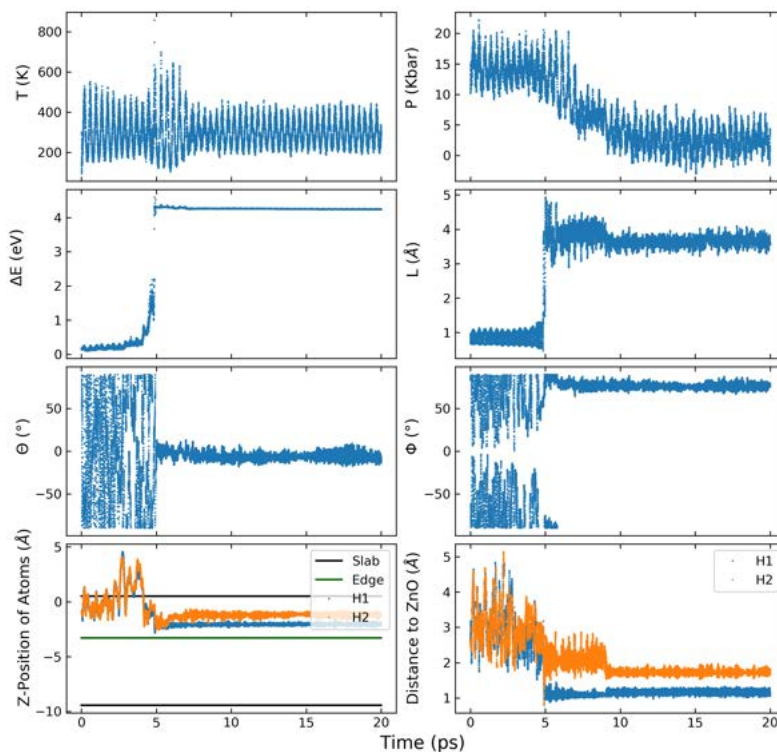
Figure 4.24: MD results for S6 with H_2

(a) t = 4.83ps   (b) t = 4.89ps
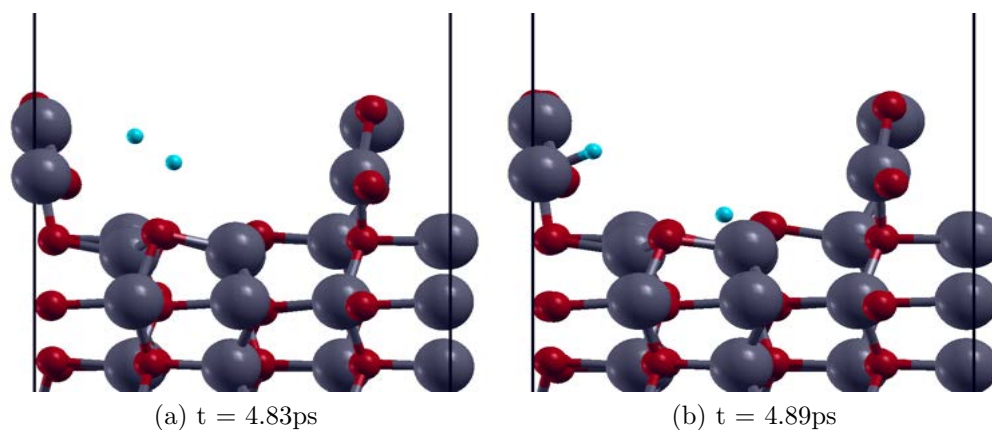
Figure 4.25: H_2 breaking its bond with edge-surface of S6
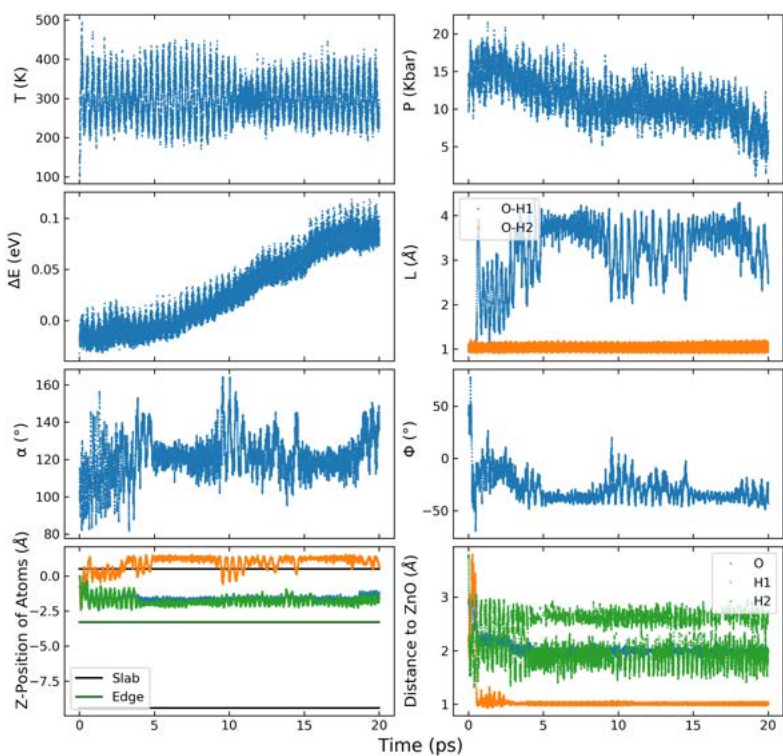
Figure 4.26: MD results for S6 with H_2O

(a) t = 5.30ps   (b) t = 5.70ps
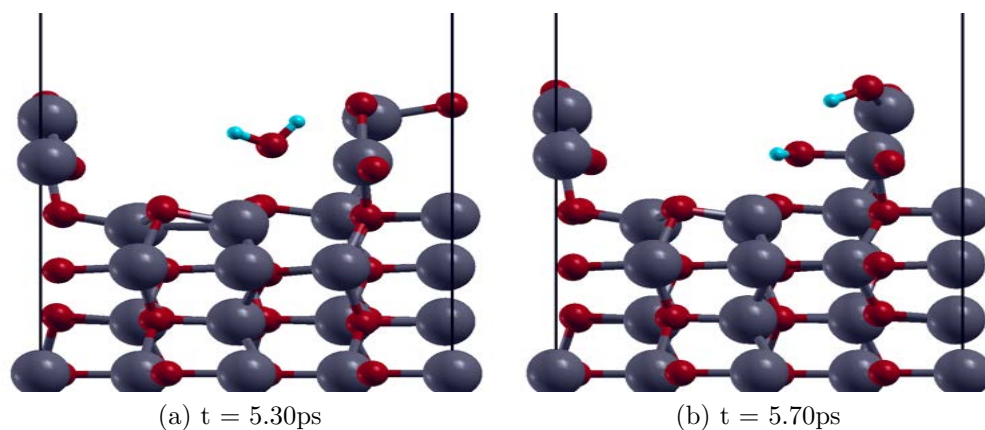
Figure 4.27: H_2O breaking its bonds with edge-surface of S6

4.2.2.3 $11\bar{2}0$-Edge-$\bar{1}2\bar{1}0$ Surface

As found in the $11\bar{2}0$ dimer-defect surface (S3), the $11\bar{2}0$-Edge-$\bar{1}2\bar{1}0$ Surface (S8) showcased bond-breaking of H_2 and weak interactions of O_2 with the surface. In figures 4.28-4.29 we see the H_2 bond being broken at the edge surface, not at the wall of the defect. The O2 run (figures 4.30-4.31) show similar weak interactions of O_2 with the surface as seen before. However, there is a clear preference for the O_2 molecule to stay near the wall of the edge-defect.
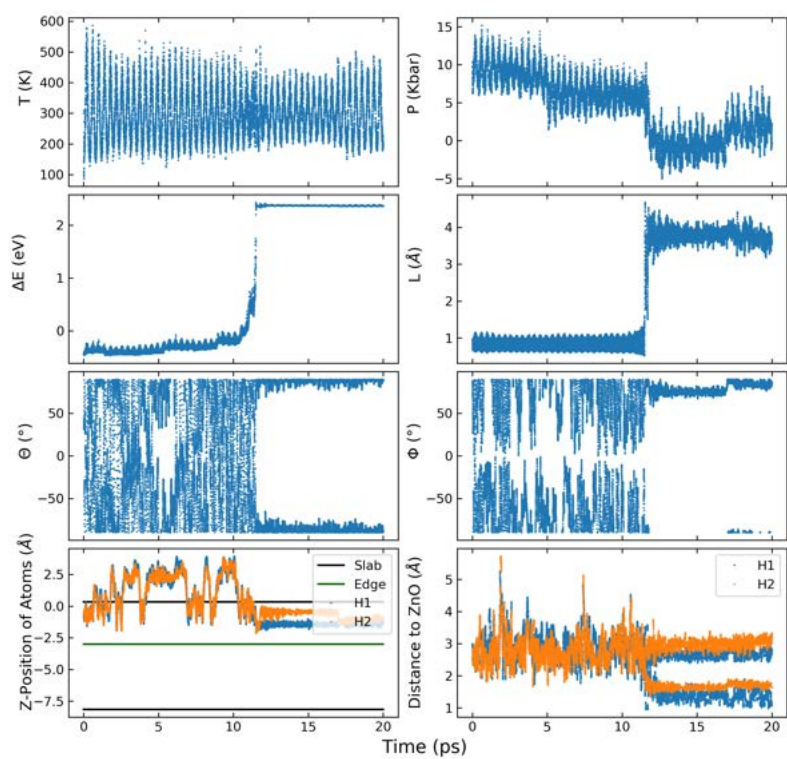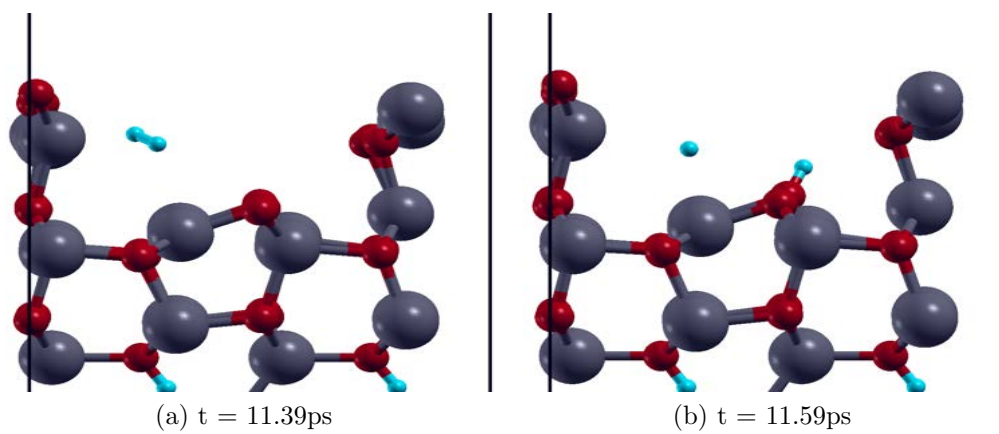
Figure 4.28: MD results for S8 with H_2

(a) t = 11.39ps

(b) t = 11.59ps

Figure 4.29: H_2 breaking its bond with edge-surface of S8
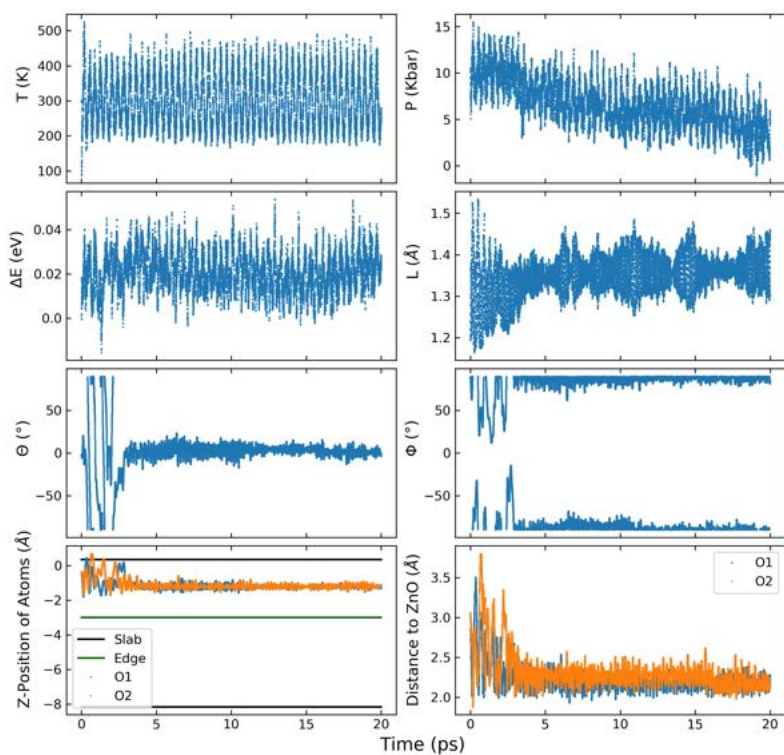
Figure 4.30: MD results for S8 with O_2

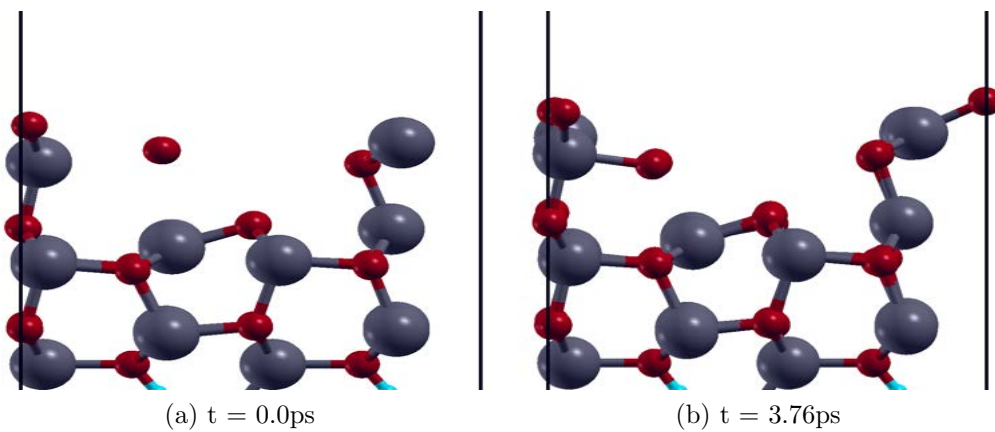(a) t = 0.0ps

(b) t = 3.76ps

Figure 4.31: O_2 weak interaction with edge-surface of S8

4.2.3 Discussion of MD results

From our CPMD simulations, we have established the potential for ZnO as a catalyst in FTS. With both the dimer and edge-defect surfaces, there were many cases of bond-

48

breaking and adsorption. This is particularly true with H_2, which is a vital component in all four of the main FTS reactions. There were also plenty of cases of weak-interactions between molecules and the defect sites, which under the right conditions may lead to adsorption and bond-breaking. Nearly all of the defect surfaces showcased the ability to break bonds and adsorb molecules, which is a promising start. However, for these non-polar surfaces of ZnO to effectively utilized, the catalytic rates need to be improved upon. In terms of what can be tested with further MD simulations, there are a few options available. All the CPMD simulations were ran at a temperature of 300K, the catalytic rates of these surfaces could change drastically with a change in termperature. For the molecules which only showed weak interactions with the surfaces, a change in temperature could result in adsorption or bond breaking.

Other options for increasing the catalytic rates of the ZnO surfaces would be to add promoters. As previously mentioned, promoters have been used extensively in FTS research; however, there has not been much research on promoters specifically for ZnO catalytic surfaces. Even though ZnO promoters have not been researched for FTS, there has been work on Cu-based catalysts doped with ZnO[50;51;52] that show that metal-oxide based promoters (ZnO) have been beneficial to the catalytic activity of these Cu-based catalysts. As seen in Chapter 1, Cu has been used as a promoter in FTS extensively. With the evidence that Cu and ZnO complement each other, promoting ZnO with Cu could be an effective way of improving catalytic rates.

From the results of this project, there is definietly promise for ZnO as an FTS catalyst. Out of the eight surfaces, four of them broke the bonds of H_2, and all of the surfaces showcase weak interactions with at least one of the other molecules, CO being the most common. The interactions between the surfaces and H_2/CO show that the four main reactions of FTS (equations 1.1-1.4) are probable over ZnO, given the right conditions. From Appendix E there is also much data on the interactions between CH_3Cl and CH_4 with the surfaces, which were not covered in the body of this

paper but could be utilized for future studies. The data from the CH_3Cl, CH_4 and all of the other molecules gives us a very good understanding of the van der Waal's interactions and adsorption properties of these non-polar ZnO surfaces. Changing the initial conditions of the MD simulations like temperature, or promoting the ZnO surface with Cu or another effective material could also improve our understanding of these materials. This project provided a good framework for understanding the dynamics of molecules over non-polar syngas, and gives us a good starting point for future CPMD and DFT reserach on these materials in order to create an effective FTS catalyst.

CHAPTER V

Other related work

From this study on FTS with ZnO surface, we have created a good framework for studying adosrption via CPMD. This same framework can be used in future reserach to study FTS or other realted processes over a multiude of different surfaces and materials. One project that I am currently working on is studying how silicon-nanotubes interact with various atomospheric molecules in order to test the effectiveness of these materials in real-world situations. One component of this project involves using the MD fomalism created for the ZnO study in order to see how various molecules interact with pristine and defect silicon-nanotubes. The reserach done on ZnO described in this paper was vital in starting this silicon-nanotube project, as the MD in the nanotube project utilizes much of the same formalism that was created over much of my time at OSU. The format of the optimizations, input-files, and pythons scripts described in Appendices A-C have been vital in the silicon-nanotubes project. My analysis method for the electrostatic potential and dissassociation energy plots have also be utilized for silicon-nanotubes. The CPMD formalism that I have created during my time here at OSU can also be used by future members of the Borunda group in their own reserach projects.

I have also been involved in research regarding photovoltaics, specifically metalhalide perovskites. I have been apart of a reserach team here at OSU headed by Dr. Borunda which studies how perovskites can function as deep-space photovoltaic devices. My current reserach involves studying how to properly calculate the defect formation energies of various metal-hailde perovskites using the Siesta package. My

work on CPMD in Siesta was vital in understanding the program as a whole, and as a result improved my research efficiency for the perovskite project. I will continue to work on the silicon-nanotubes and solar-cell perovskite projects in the coming months, and use the expertise gained from studying FTS on ZnO surfaces to continue to study the physical properties of advanced materials.

References

[1] A. E. Outlook, "Us energy information administration: Washington," 2013.

[2] Q. Zhang, J. Kang, and Y. Wang, "Development of novel catalysts for fischer–tropsch synthesis: tuning the product selectivity," *ChemCatChem*, vol. 2, no. 9, pp. 1030–1058, 2010.

[3] G. P. Van Der Laan and A. Beenackers, "Kinetics and selectivity of the fischer–tropsch synthesis: a literature review," *Catalysis Reviews*, vol. 41, no. 3-4, pp. 255–318, 1999.

[4] A. Alayat, E. Echeverria, D. N. McIlroy, and A. G. McDonald, "Enhancement of the catalytic performance of silica nanosprings (ns)-supported iron catalyst with copper, molybdenum, cobalt and ruthenium promoters for fischer-tropsch synthesis," *Fuel Processing Technology*, vol. 177, pp. 89–100, 2018.

[5] H. Mahmoudi, M. Mahmoudi, O. Doustdar, H. Jahangiri, A. Tsolakis, S. Gu, and M. LechWyszynski, "A review of fischer tropsch synthesis process, mechanism, surface chemistry and catalyst formulation," *Biofuels Engineering*, vol. 2, no. 1, pp. 11–31, 2017.

[6] D. Leckel, "Diesel production from fischer- tropsch: the past, the present, and new concepts," *Energy & Fuels*, vol. 23, no. 5, pp. 2342–2358, 2009.

[7] A. Sandoval, A. Gómez-Cortés, R. Zanella, G. Díaz, and J. M. Saniger, "Gold nanoparticles: support effects for the wgs reaction," *Journal of Molecular Catalysis A: Chemical*, vol. 278, no. 1-2, pp. 200–208, 2007.

[8] A. P. Steynberg and H. G. Nel, "Clean coal conversion options using fischer–tropsch technology," *Fuel*, vol. 83, no. 6, pp. 765–770, 2004.

[9] A. De Klerk, "Environmentally friendly refining: Fischer–tropsch versus crude oil," *Green Chemistry*, vol. 9, no. 6, pp. 560–565, 2007.

[10] C. Knottenbelt, "Mossgas "gas-to-liquid" diesel fuels—an environmentally friendly option," *Catalysis Today*, vol. 71, no. 3-4, pp. 437–445, 2002.

[11] G. Maschio, A. Lucchesi, and G. Stoppato, "Production of syngas from biomass," *Bioresource Technology*, vol. 48, no. 2, pp. 119–126, 1994.

[12] G. Jacobs, T. K. Das, Y. Zhang, J. Li, G. Racoillet, and B. H. Davis, "Fischer–tropsch synthesis: support, loading, and promoter effects on the reducibility of cobalt catalysts," *Applied Catalysis A: General*, vol. 233, no. 1-2, pp. 263–281, 2002.

[13] H. Karaca, O. V. Safonova, S. Chambrey, P. Fongarland, P. Roussel, A. Griboval-Constant, M. Lacroix, and A. Y. Khodakov, "Structure and catalytic performance of pt-promoted alumina-supported cobalt catalysts under realistic conditions of fischer–tropsch synthesis," *Journal of catalysis*, vol. 277, no. 1, pp. 14–26, 2011.

[14] A. D. McNaught, A. Wilkinson, *et al.*, *Compendium of chemical terminology*, vol. 1669. Blackwell Science Oxford, 1997.

[15] H. Schulz, "Short history and present trends of fischer–tropsch synthesis," *Applied Catalysis A: General*, vol. 186, no. 1-2, pp. 3–12, 1999.

[16] V. Rao, G. Stiegel, G. Cinquegrane, and R. Srivastava, "Iron-based catalysts for slurry-phase fischer-tropsch process: Technology review," *Fuel processing technology*, vol. 30, no. 1, pp. 83–107, 1992.

[17] H. Xiong, M. A. Motchelaho, M. Moyo, L. L. Jewell, and N. J. Coville, "Effect of group i alkali metal promoters on fe/cnt catalysts in fischer–tropsch synthesis," *Fuel*, vol. 150, pp. 687–696, 2015.

[18] A. Cao, J. Schumann, T. Wang, L. Zhang, J. Xiao, P. Bothra, Y. Liu, F. Abild-Pedersen, and J. K. Nørskov, "Mechanistic insights into the synthesis of higher alcohols from syngas on cuco alloys," *ACS Catalysis*, vol. 8, no. 11, pp. 10148–10155, 2018.

[19] M. Kurtz, J. Strunk, O. Hinrichsen, M. Muhler, K. Fink, B. Meyer, and C. Wöll, "Active sites on oxide surfaces: Zno-catalyzed synthesis of methanol from co and h2," *Angewandte Chemie International Edition*, vol. 44, no. 18, pp. 2790–2794, 2005.

[20] R.-J. Liu, Y. Xu, Y. Qiao, Z.-H. Li, and X.-B. Ma, "Factors influencing the fischer–tropsch synthesis performance of iron-based catalyst: Iron oxide dispersion, distribution and reducibility," *Fuel Processing Technology*, vol. 139, pp. 25–32, 2015.

[21] H. Agarwal, S. V. Kumar, and S. Rajeshkumar, "A review on green synthesis of zinc oxide nanoparticles–an eco-friendly approach," *Resource-Efficient Technologies*, vol. 3, no. 4, pp. 406–413, 2017.

[22] R. Kováčik, B. Meyer, and D. Marx, "F centers versus dimer vacancies on zno surfaces: characterization by stm and sts calculations," *Angewandte Chemie International Edition*, vol. 46, no. 26, pp. 4894–4897, 2007.

[23] S. Polarz, J. Strunk, V. Ischenko, M. W. Van den Berg, O. Hinrichsen, M. Muhler, and M. Driess, "On the role of oxygen defects in the catalytic performance of zinc oxide," *Angewandte Chemie International Edition*, vol. 45, no. 18, pp. 2965–2969, 2006.

[24] H. Wilmer, M. Kurtz, K. Klementiev, O. Tkachenko, W. Grünert, O. Hinrichsen, A. Birkner, S. Rabe, K. Merz, M. Driess, *et al.*, "Methanol synthesis over zno: A structure-sensitive reaction?," *Physical Chemistry Chemical Physics*, vol. 5, no. 20, pp. 4736–4742, 2003.

[25] T. Becker, C. Boas, U. Burghaus, and C. Wöll, "Adsorption probability of co on a metal oxide: The case of oxygen-terminated zno and the influence of defects," *Physical Review B*, vol. 61, no. 7, p. 4538, 2000.

[26] T. Becker, M. Kunat, C. Boas, U. Burghaus, and C. Wöll, "Adsorption dynamics of co on the polar surfaces of zno," *The Journal of Chemical Physics*, vol. 113, no. 15, pp. 6334–6343, 2000.

[27] T. Becker, M. Kunat, C. Boas, U. Burghaus, C. Wöll, *et al.*, "Interaction of hydrogen with metal oxides: the case of the polar zno (0 0 0 1) surface," *Surface science*, vol. 486, no. 3, pp. L502–L506, 2001.

[28] O. Dulub, L. A. Boatner, and U. Diebold, "Stm study of the geometric and electronic structure of zno (0001)-zn,(0001)-o,(1010), and (1120) surfaces," *Surface Science*, vol. 519, no. 3, pp. 201–217, 2002.

[29] M. Králik, "Adsorption, chemisorption, and catalysis," *Chemical Papers*, vol. 68, no. 12, pp. 1625–1638, 2014.

[30] Y. Qi, C. Ledesma, J. Yang, X. Duan, Y.-A. Zhu, A. Holmen, and D. Chen, "Adsorption energy-driven carbon number-dependent olefin to paraffin ratio in cobalt-catalyzed fischer-tropsch synthesis," *Journal of Catalysis*, vol. 349, pp. 110–117, 2017.

[31] J. Cheng, T. Song, P. Hu, C. M. Lok, P. Ellis, and S. French, "A density functional theory study of the α-olefin selectivity in fischer–tropsch synthesis," *Journal of catalysis*, vol. 255, no. 1, pp. 20–28, 2008.

[32] S. Barraza-Lopez and T. P. Kaloni, "Water splits to degrade two-dimensional group-iv monochalcogenides in nanoseconds," *ACS central science*, vol. 4, no. 10, pp. 1436–1446, 2018.

[33] J. M. Soler, E. Artacho, J. D. Gale, A. García, J. Junquera, P. Ordejón, and D. Sánchez-Portal, "The siesta method for ab initio order-n materials simulation," *Journal of Physics: Condensed Matter*, vol. 14, no. 11, p. 2745, 2002.

[34] A. Szabo and N. Ostlund, "Modern quantum chemistry. macgraw-hill," 1989.

[35] M. Born and R. Oppenheimer, "Zur quantentheorie der molekeln," *Annalen der physik*, vol. 389, no. 20, pp. 457–484, 1927.

[36] R. M. Martin, *Electronic structure: basic theory and practical methods.* Cambridge university press, 2020.

[37] P. Hohenberg and W. Kohn, "Inhomogeneous electron gas," *Physical review*, vol. 136, no. 3B, p. B864, 1964.

[38] W. Kohn and L. J. Sham, "Self-consistent equations including exchange and correlation effects," *Physical review*, vol. 140, no. 4A, p. A1133, 1965.

[39] D. Natelson, *Nanostructures and nanotechnology.* Cambridge University Press, 2015.

[40] R. Car and M. Parrinello, "Unified approach for molecular dynamics and density-functional theory," *Physical review letters*, vol. 55, no. 22, p. 2471, 1985.

[41] M. Boero and A. Oshiyama, "Car–parrinello molecular dynamics encyclopedia of nanotechnology," 2015.

[42] N. Troullier and J. L. Martins, "Efficient pseudopotentials for plane-wave calculations," *Physical review B*, vol. 43, no. 3, p. 1993, 1991.

[43] H. Rydberg, M. Dion, N. Jacobson, E. Schröder, P. Hyldgaard, S. Simak, D. C. Langreth, and B. I. Lundqvist, "Van der waals density functional for layered structures," *Physical review letters*, vol. 91, no. 12, p. 126402, 2003.

[44] V. R. Cooper, "Van der waals density functional: An appropriate exchange functional," *Physical Review B*, vol. 81, no. 16, p. 161104, 2010.

[45] A. Garcıa, "Atom user manual," 2008.

[46] H. M. Chen, C. K. Chen, Y.-C. Chang, C.-W. Tsai, R.-S. Liu, S.-F. Hu, W.-S. Chang, and K.-H. Chen, "Quantum dot monolayer sensitized zno nanowire-array photoelectrodes: true efficiency for water splitting," *Angewandte Chemie*, vol. 122, no. 34, pp. 6102–6105, 2010.

[47] X. Yang, A. Wolcott, G. Wang, A. Sobo, R. C. Fitzmorris, F. Qian, J. Z. Zhang, and Y. Li, "Nitrogen-doped zno nanowire arrays for photoelectrochemical water splitting," *Nano letters*, vol. 9, no. 6, pp. 2331–2336, 2009.

[48] S. Hernández, D. Hidalgo, A. Sacco, A. Chiodoni, A. Lamberti, V. Cauda, E. Tresso, and G. Saracco, "Comparison of photocatalytic and transport properties of tio 2 and zno nanostructures for solar-driven water splitting," *Physical Chemistry Chemical Physics*, vol. 17, no. 12, pp. 7775–7786, 2015.

[49] K. Maeda, T. Takata, M. Hara, N. Saito, Y. Inoue, H. Kobayashi, and K. Domen, "Gan: Zno solid solution as a photocatalyst for visible-light-driven overall water splitting," *Journal of the American Chemical Society*, vol. 127, no. 23, pp. 8286–8287, 2005.

[50] S. Sanches, J. H. Flores, R. De Avillez, and M. P. Da Silva, "Influence of preparation methods and zr and y promoters on cu/zno catalysts used for methanol steam reforming," *International journal of hydrogen energy*, vol. 37, no. 8, pp. 6572–6579, 2012.

[51] G.-S. Wu, D.-S. Mao, G.-Z. Lu, Y. Cao, and K.-N. Fan, "The role of the promoters in cu based catalysts for methanol steam reforming," *Catalysis letters*, vol. 130, no. 1-2, pp. 177–184, 2009.

[52] M. Behrens, F. Studt, I. Kasatkin, S. Kühl, M. Hävecker, F. Abild-Pedersen, S. Zander, F. Girgsdies, P. Kurr, B.-L. Kniep, *et al.*, "The active site of methanol synthesis over cu/zno/al2o3 industrial catalysts," *Science*, vol. 336, no. 6083, pp. 893–897, 2012.

APPENDIX A

Siesta Optimiztions

Before all major calculations were carried out through Siesta, optimization tests were done for both geometry relaxation (Conjugate gradient) and MD calculations. Figures A.1-A.3 represent optmization test for relaxation, and A.4-A.6 for MD. For the relaxation plots, the optimization of the meshcutoff, unit cell size, and force convergence threshold were done with respect to the total energy and walltime of the calculation. An optimized value for each would have the shortest possible walltime at an energy value that has asymptotically converged to a certain value. The meshcutoff value represents the finess of the 3D grid in which Siesta runs all its plane wave calculations, the lower to meshcutoff the finer the grid. The optmized value used found for meshcutoff was around 200Ry. The unit cell size is the size in Åof the simulation box, this optimization was used for the dissasociation energy calculations. The unit cell value chosen was a 30x30x30 cell. The force convergence threshold (otherwise known as the max force tolerance) is the value of the atomic force per Åthat is required for a geometry relaxation calculation to be converged. The value chosen for this project is 0.02 ev/ Å .

Figures A.4-A.6 optmize the denisty matrix (DM) mixing weight, pulay number, and number kick. The DM mixing weight value represents the percentage of the output density matrix to be used in the input of the new density matrix. The mixing weight along with pulay number and number kick directly effect the SCF cycle of the Siesta calculations. The mixing weight chosen for the MD calculations was 0.15. The pulay number represents how non-linear the density matrix mixing will be, where a pulay number of 0 or 1 is linear mixing. The value chosen was 10. The number kick represents hw many SCF cycles a non-linear pulay mixing goes through before the SCF goes back to linear mixing. The value chosen for this project was 30; however, in general the SCF cycles never got that high.
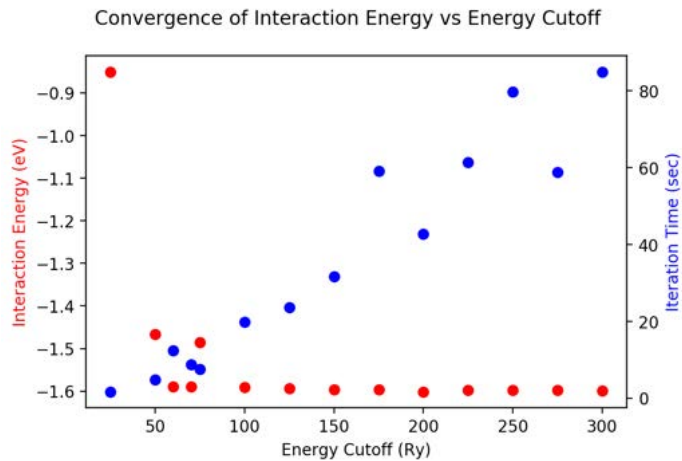
Figure A.1: Meshcutoff vs Walltime/Total Energy
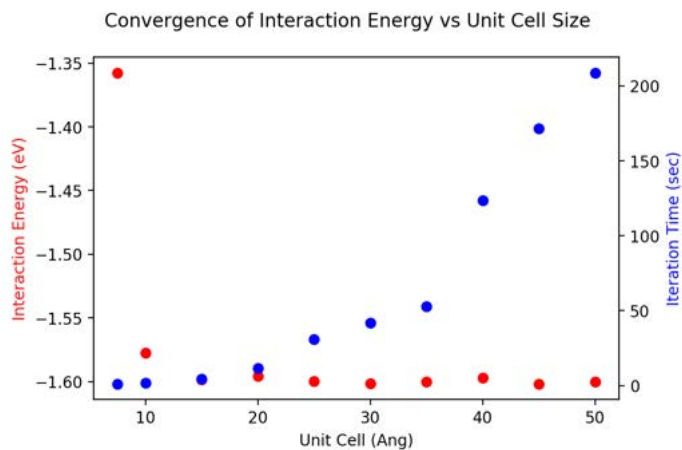
Figure A.2: Unit Cell Size vs Walltime/Total Energy
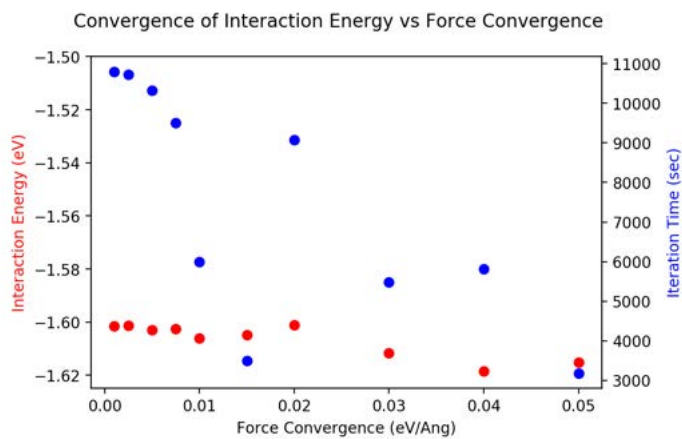
Figure A.3: Force Convergence Threshold vs Walltime/Total Energy
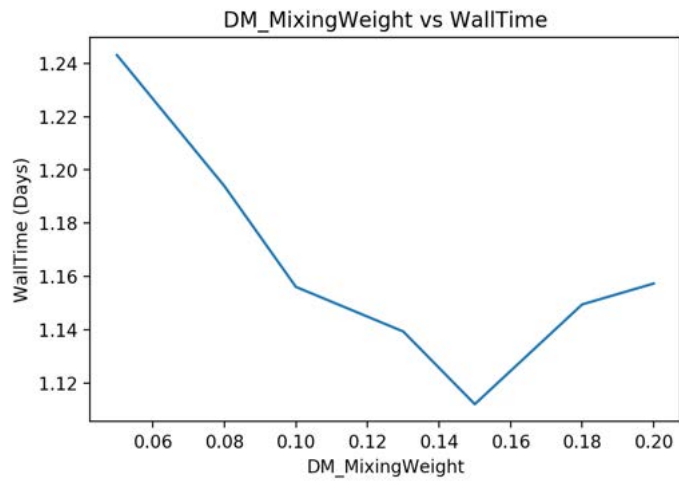
Figure A.4: DM Mixing Weight vs Walltime
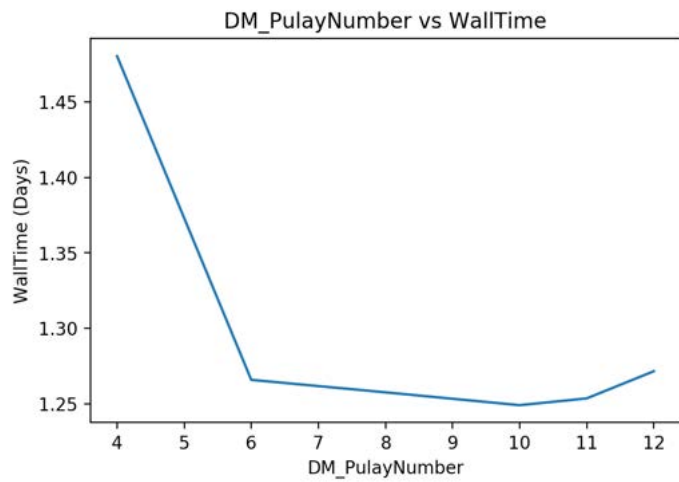
Figure A.5: DM Pulay Number vs Walltime
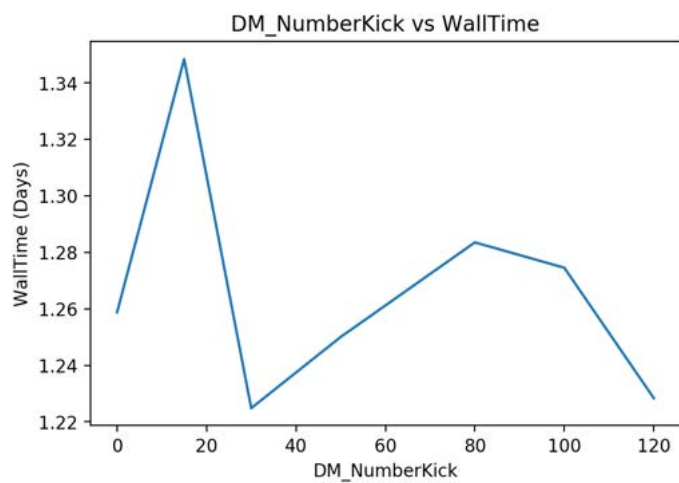
Figure A.6: DM Number Kick vs Walltime

APPENDIX B

Siesta FDF files

Example FDF (Siesta input files) data for the MD and slab relaxation calculations
are listed below.

The following contains all the input variables for the Siesta FDF files that was
used to relax S1:

```
SystemName          1120-Slab-Defect
SystemLabel         1120-Slab-Defect


NumberOfAtoms       78
LatticeConstant     20    Ang


PAO.EnergyShift 0.005 Ry


%block LatticeVectors
0.5206 0.0000 0.0000
0.0000 0.6588 0.0000
0.0000 0.0000 1.0000
%endblock LatticeVectors


XC.functional VDW
XC.authors C09
MeshCutoff   200 Ry
MaxSCFIterations 200


NumberOfSpecies      3
%block ChemicalSpeciesLabel
 1  30  Zn
 2  8  O
 3  1  H
%endblock ChemicalSpeciesLabel
%block AtomicMass
 1  65.380
 2  15.999
 3  1.008
%endblock AtomicMass
%block Ps.lmax
 Zn  2
```

```
 O  1
 H  0
%endblock Ps.lmax

AtomicCoordinatesFormat   Ang
%block AtomicCoordinatesAndAtomicSpecies
        3.102290000    7.162600000  -5.039460000 2
       -0.086550000    7.162600000  -5.039460000 1
        3.102290000    3.922600000  -5.039460000 2
       -0.086550000    3.922600000  -5.039460000 1
        3.013903477    8.837774510  -2.234661839 2
        2.348949323    8.836650749  -4.153928197 1
        0.406091322    8.836703315  -3.993814063 2
       -0.189427679    8.837725717  -2.000157098 1
        3.014855173    5.543757047  -2.186539429 2
        2.343683414    5.542750013  -4.093977711 1
        0.403804297    5.542669445  -3.941915188 2
       -0.189906894    5.543672195  -1.947228143 1
        2.208419558    7.200251483  -1.506737907 1
        0.379652922    7.202029582  -1.114695182 2
        3.095462793    7.144652231  -6.030951589 3
       -0.066748651    7.159206947  -6.660670286 3
        3.095784864    3.942344025  -6.030958250 3
       -0.067356548    3.927568883  -6.660860248 3
        3.102290000   13.750600000  -5.039460000 2
       -0.086550000   13.750600000  -5.039460000 1
        3.102290000   10.510600000  -5.039460000 2
       -0.086550000   10.510600000  -5.039460000 1
        3.013903069   15.425725364  -2.234668702 2
        2.348967146   15.424737190  -4.153881557 1
        0.406089718   15.424740071  -3.993824838 2
       -0.189448145   15.425650772  -2.000108289 1
        3.014857484   12.131772191  -2.186572673 2
        2.343685891   12.130569786  -4.094075554 1
        0.403811746   12.130649285  -3.941933780 2
       -0.189903080   12.131665544  -1.947282713 1
        2.208424059   13.788197072  -1.506676411 1
        0.379659803   13.789993858  -1.114620896 2
        2.208415096   10.475272488  -1.506775519 1
        0.379665919   10.473275006  -1.114645628 2
        3.095462793   13.732652231  -6.030951589 3
       -0.066748651   13.747206947  -6.660670286 3
        3.095784864   10.530344025  -6.030958250 3
       -0.067356548   10.515568883  -6.660860248 3
        8.308290000    7.162600000  -5.039460000 2
```

```
        5.119450000    7.162600000   -5.039460000 1
        8.308290000    3.922600000   -5.039460000 2
        5.119450000    3.922600000   -5.039460000 1
        8.219736208    8.837775140   -2.234854483 2
        7.554651878    8.836648340   -4.154089138 1
        5.611692199    8.836701640   -3.993900766 2
        5.016434630    8.837725000   -2.000226069 1
        8.220695300    5.543757377   -2.186739149 2
        7.549415246    5.542752754   -4.094158115 1
        5.609461423    5.542668757   -3.941963106 2
        5.015966574    5.543670971   -1.947261706 1
        7.414098626    7.200243763   -1.506888172 1
        5.585353594    7.202038646   -1.114836953 2
        7.414094831    3.887230629   -1.506875990 1
        5.585350923    3.885218763   -1.114797839 2
        8.301462793    7.144652231   -6.030951589 3
        5.139251349    7.159206947   -6.660670286 3
        8.301784864    3.942344025   -6.030958250 3
        5.138643452    3.927568883   -6.660860248 3
        8.308290000   13.750600000   -5.039460000 2
        5.119450000   13.750600000   -5.039460000 1
        8.308290000   10.510600000   -5.039460000 2
        5.119450000   10.510600000   -5.039460000 1
        8.219734605   15.425725758   -2.234860935 2
        7.554668891   15.424741363   -4.154043911 1
        5.611690422   15.424738244   -3.993909296 2
        5.016413145   15.425648059   -2.000173000 1
        8.220699103   12.131771890   -2.186774205 2
        7.549411634   12.130567516   -4.094260942 1
        5.609468582   12.130648421   -3.941978521 2
        5.015966843   12.131663928   -1.947310235 1
        7.414103149   13.788186882   -1.506826135 1
        5.585359074   13.790001335   -1.114759227 2
        7.414093071   10.475282740   -1.506926403 1
        5.585364912   10.473263635   -1.114785720 2
        8.301462793   13.732652231   -6.030951589 3
        5.139251349   13.747206947   -6.660670286 3
        8.301784864   10.530344025   -6.030958250 3
        5.138643452   10.515568883   -6.660860248 3
%endblock AtomicCoordinatesAndAtomicSpecies

%block kgrid_Monkhorst_Pack
 8 0 0 0.0
 0 8 0 0.0
 0 0 1 0.0
```

```
%endblock kgrid_Monkhorst_Pack

MD.TypeOfRun CG
MD.NumCGsteps 200
MD.MaxForceTol 0.02 eV/Ang

DM.MixingWeight 0.1

WriteCoorXmol .true.

save-rho T
save-delta-rho T
save-total-potential T
save-neutral-atom-potential T
save-hs T
```

The following contains all the input variables for the Siesta FDF that was used for the MD simulation of an H2 molecule over S1:

```
SystemName          MDSlab1
SystemLabel         MDSlab1

## Lattice, Element and Atomic Structure Data

NumberOfAtoms       80
NumberOfSpecies     3

LatticeConstant     20    Ang
%block LatticeVectors
0.5206 0.0000 0.0000
0.0000 0.6588 0.0000
0.0000 0.0000 1.0000
%endblock LatticeVectors

%block ChemicalSpeciesLabel
 1  30  Zn
 2  8   O
 3  1   H
%endblock ChemicalSpeciesLabel
%block AtomicMass
```

```
 1  65.380
 2  15.999
 3   1.008
%endblock AtomicMass
%block Ps.lmax
 Zn  2
 O  1
 H  0
%endblock Ps.lmax

AtomicCoordinatesFormat   Ang
%block AtomicCoordinatesAndAtomicSpecies
3.102290 7.162600 -5.039460 2
-0.086550 7.162600 -5.039460 1
3.102290 3.922600 -5.039460 2
-0.086550 3.922600 -5.039460 1
3.031225 8.847592 -2.209306 2
2.348949 8.836651 -4.153928 1
0.363264 8.833933 -3.990293 2
-0.058053 8.838680 -2.052407 1
2.963852 5.360348 -2.115920 2
2.485449 5.544224 -4.052852 1
0.417335 5.519520 -3.865998 2
-0.167588 5.546289 -1.944340 1
2.255843 7.082439 -1.499504 1
0.325951 7.164310 -0.898175 2
3.095463 7.144652 -6.030952 3
-0.066749 7.159207 -6.660670 3
3.095785 3.942344 -6.030958 3
-0.067357 3.927569 -6.660860 3
3.102290 13.750600 -5.039460 2
-0.086550 13.750600 -5.039460 1
3.102290 10.510600 -5.039460 2
-0.086550 10.510600 -5.039460 1
3.042696 15.419898 -2.268289 2
2.348967 15.424737 -4.153882 1
0.336524 15.441356 -3.973223 2
-0.057144 15.425429 -2.054162 1
3.092908 12.166830 -2.181265 2
2.484649 12.133115 -4.056717 1
0.460899 12.135014 -3.878212 2
-0.169116 12.133527 -1.942473 1
2.254369 13.783367 -1.498680 1
0.341859 13.870798 -0.882284 2
2.253752 10.591951 -1.498248 1
```

```
0.367432 10.476648 -0.915312 2
3.095463 13.732652 -6.030952 3
-0.066749 13.747207 -6.660670 3
3.095785 10.530344 -6.030958 3
-0.067357 10.515569 -6.660860 3
8.308290 7.162600 -5.039460 2
5.119450 7.162600 -5.039460 1
8.308290 3.922600 -5.039460 2
5.119450 3.922600 -5.039460 1
8.276787 8.886624 -2.242256 2
7.554652 8.836648 -4.154089 1
5.574055 8.837801 -3.990981 2
5.146736 8.838869 -2.052545 1
8.322987 5.576035 -2.206824 2
7.576899 5.544691 -4.057654 1
5.600844 5.547309 -3.884718 2
5.029695 5.544179 -1.942013 1
7.460498 7.194112 -1.498430 1
5.598524 7.207981 -0.916159 2
7.458833 4.005194 -1.498238 1
5.632047 3.880751 -0.909852 2
8.301463 7.144652 -6.030952 3
5.139251 7.159207 -6.660670 3
8.301785 3.942344 -6.030958 3
5.138643 3.927569 -6.660860 3
8.308290 13.750600 -5.039460 2
5.119450 13.750600 -5.039460 1
8.308290 10.510600 -5.039460 2
5.119450 10.510600 -5.039460 1
8.315438 15.508801 -2.219052 2
7.554669 15.424741 -4.154044 1
5.596227 15.421998 -3.995352 2
5.144506 15.427411 -2.052545 1
8.299553 12.192710 -2.228405 2
7.576422 12.132748 -4.057982 1
5.588236 12.127189 -3.885860 2
5.036585 12.133176 -1.941911 1
7.460506 13.782714 -1.498390 1
5.607279 13.786592 -0.905382 2
7.460153 10.593160 -1.498388 1
5.592205 10.469808 -0.916849 2
8.301463 13.732652 -6.030952 3
5.139251 13.747207 -6.660670 3
8.301785 10.530344 -6.030958 3
5.138643 10.515569 -6.660860 3
```

```
1.8868559960 5.5590057778 0.7898579432 3
1.6321559962 6.2195057778 0.7898579432 3
%endblock AtomicCoordinatesAndAtomicSpecies

%block GeometryConstraints
   position  from 1 to 4
   position  from 15 to 22
   position  from 35 to 42
   position  from 55 to 62
   position  from 75 to 78
%endblock GeometryConstraints
```

Kgrid

```
%block kgrid_Monkhorst_Pack
 2 0 0 0.0
 0 2 0 0.0
 0 0 1 0.0
%endblock kgrid_Monkhorst_Pack
```

Functional Data

```
XC.functional VDW
XC.authors C09
```

Optimization Flags

```
PAO.EnergyShift 0.005 Ry
MeshCutoff  200 Ry
MaxSCFIterations 200
DM.NumberPulay 10
DM.MixingWeight 0.15
DM.NumberKick 30
```

MD Description Flags

```
MD.TypeOfRun Nose
MD.NoseMass 1500 Ry*fs**2
MD.FinalTimeStep 20000
MD.InitialTemperature 300.0 K
MD.TargetTemperature 300.0 K
```

```
## Output Data

WriteMDhistory .true.
WriteForces .true.
WriteCoorInitial .true.
WriteCoorStep .true.
WriteMDXmol .true.
WriteCoorXmol .true.
SaveElectrostaticPotential .true.

save-rho T
save-delta-rho T
save-total-potential T
save-neutral-atom-potential T
save-hs T
```

APPENDIX C

Python Scripts

The following is the script I created to pull all the relevant data from the Siesta output files. The Siesta output files needed for this code are the ANI, MD-CAR, and the MDE. For the MDE-file, it is output from Siesta in microsoft-access form, it must first be saved in a text file to run this code. This particular code is used specifically for any two atom molecule (CO, O2, and H2). The codes used for the three-atom and five-atom molecules follow the same format with slight modifications.

```python
# -*- coding: utf-8 -*-
"""
Created on Fri Sep  4 13:54:32 2020

@author: chari
"""

# Full 2_atom Plotter

#MDE plotter file
import numpy as np
import matplotlib.pyplot as plt
import math
import matplotlib.ticker as ticker

# directories
Slab="8"
Run="H2_defectR"
file_MDE="MDSlab"+Slab+"_txt.txt"
file_ANI = "MDSlab"+Slab+".ANI"

open_MDE = "S"+Slab+"/"+Run+"/"+file_MDE

open_ANI = "S"+Slab+"/"+Run+"/"+file_ANI

open_MD_CAR = "S"+Slab+"/"+Run+"/"+"MDSlab"+Slab+".MD_CAR"

save = "S"+Slab+"/"+Run+"/"

num_MD_atoms = 2
MD_atom1 = "H1"
MD_atom2 = "H2"

molecule = "H2"
```

```python
#
time_steps = np.array([])
temperature = np.array([])
pressure = np.array([])
energy = np.array([])
#
Read_MDE = open(open_MDE,"r")
lines = Read_MDE.readlines()[1:]
time_steps = np.array([])
temperature = np.array([])
pressure = np.array([])
energy = np.array([])
for aline in lines:
    value = aline.split()
    time_steps = np.append(time_steps,float(value[0]))
    temperature = np.append(temperature,float(value[1]))
    energy = np.append(energy,float(value[3]))
    pressure = np.append(pressure,float(value[5]))


Read_MDE.close()


#
Read_ANI = open(open_ANI,"r")
lines = Read_ANI.readlines()
num_atoms = int(lines[0])
Read_ANI.close()


multi = [num_atoms+(n)*(num_atoms+num_MD_atoms) for n in range(0,19999+1)]

index1 = np.array([])
index2 = np.array([])

A1_position = np.zeros([20000,3])
A2_position = np.zeros([20000,3])

# Code

count = 0

Read_ANI = open(open_ANI,"r")
lines = Read_ANI.readlines()

for i in range(len(lines)-1):
    A1 = multi[count]
    if i == A1:
        index1 = np.append(index1,lines[A1])
    else:
        continue
    count = count +1

count = 0
for j in range(len(lines)):
```

72

```
            A2 = 1 + multi[count]
            if j == A2:
                index2 = np.append(index2,lines[A2])
            else:
                continue
            count = count + 1


Read_ANI.close()


count_pos = 0
for i in index1:
    value = i.split()
    A1_position[count_pos,0] = value[1]
    A1_position[count_pos,1] = value[2]
    A1_position[count_pos,2] = value[3]


    count_pos = count_pos +1




count_pos = 0
for j in index2:
    value = j.split()
    A2_position[count_pos,0] = value[1]
    A2_position[count_pos,1] = value[2]
    A2_position[count_pos,2] = value[3]


    count_pos = count_pos +1


time_range = np.arange(1,20001)


L_A1A2 = np.array([])


for i in range(len(A1_position)):
    L = np.sqrt((A2_position[i,0]-A1_position[i,0])**2 + (A2_position[i,1]-A1_position[i,1])**2 + (A2_position[i,2]-A1_position[i,2])**2)
    L_A1A2 = np.append(L_A1A2,L)



Z_vals_Slab = np.array([])
Read_ANI = open(open_ANI,"r")
lines = Read_ANI.readlines()[2:multi[0]]
for aline in lines:
    value = aline.split()
    Z_vals_Slab = np.append(Z_vals_Slab,float(value[3]))
Read_ANI.close()


high_val = (0)*(time_range)+(np.max(Z_vals_Slab))
low_val = (0)*(time_range)+(np.min(Z_vals_Slab))


defR_val_S5 = (0)*(time_range)+(-2.8915570000)
defR_val_S6 = (0)*(time_range)+(-3.2959550000)
defR_val_S7 = (0)*(time_range)+(-2.6467980000)
defR_val_S8 = (0)*(time_range)+(-3.0000)


# Angles
```

```python
theta = np.array([])
phi = np.array([])


for i in range(len(A1_position[:,0])):
    numerator = A2_position[i,1] - A1_position[i,1]
    demoninator = A2_position[i,0] - A1_position[i,0]
    theta_add = math.degrees(np.arctan(numerator/demoninator))
    theta = np.append(theta,theta_add)


for i in range(len(A1_position[:,0])):
    numer = np.sqrt((A2_position[i,0]-A1_position[i,0])**2 + (A2_position[i,1]-A1_position[i,1])**2)
    denom = A2_position[i,2] - A1_position[i,2]
    phi_add = math.degrees(np.arctan(numer/denom))
    phi = np.append(phi,phi_add)


####

cell_values = np.zeros([3,3])
Read_MD_CAR = open(open_MD_CAR,"r")
linesCAR = Read_MD_CAR.readlines()[2:5]
count_CAR = 0
for aline in linesCAR:
    value = aline.split()
    cell_values[count_CAR,:] = [float(value[0]),float(value[1]),float(value[2])]
    count_CAR = count_CAR + 1


Read_MD_CAR.close()


Read_ANI = open(open_ANI,"r")
lines = Read_ANI.readlines()
num_atoms = int(lines[0])
Read_ANI.close()


multi = [num_atoms+(n)*(num_atoms+num_MD_atoms) for n in range(0,19999+1)]
start_chunk = [x - (num_atoms - num_MD_atoms) for x in multi]
end_chunk = [x + (num_MD_atoms) for x in multi]


list1 = np.zeros([num_atoms,20000])
list2 = np.zeros([num_atoms,20000])


Read_ANI = open(open_ANI,"r")
lines = Read_ANI.readlines()


count_m = 0


for j in range(len(start_chunk)):
    count_list_1 = 0
    start = start_chunk[j]
    end = end_chunk[j]
    for i in lines[start:end]:
        value = i.split()
        A1 = lines[multi[count_m]]
        A2 = lines[multi[count_m]+1]
```

```
        A1_x = np.mod(float(A1.split()[1]),cell_values[0,0])
        A1_y = np.mod(float(A1.split()[2]),cell_values[1,1])
        A1_z = float(A1.split()[3])
        A2_x = np.mod(float(A2.split()[1]),cell_values[0,0])
        A2_y = np.mod(float(A2.split()[2]),cell_values[1,1])
        A2_z = float(A2.split()[3])


        list1[count_list_1,count_m] = np.sqrt((A1_x-float(value[1]))**2 + (A1_y-float(value[2]))**2 + (A1_z-float(value[3]))**2)

        list2[count_list_1,count_m] = np.sqrt((A2_x-float(value[1]))**2 + (A2_y-float(value[2]))**2 + (A2_z-float(value[3]))**2)


        count_list_1 = count_list_1 + 1

    count_m = count_m +1

Read_ANI.close()



######
d_A1 = np.array([])
d_A2 = np.array([])

deleted_atoms = [-(num_MD_atoms)+(num_atoms)+n for n in range(0,num_MD_atoms)]

list_A1 = np.delete(list1,deleted_atoms,0)
list_A2 = np.delete(list2,deleted_atoms,0)

count_LA1 = 0
for i in range(len(list_A1[0,:])):
    lowest_A1 = float(min(list_A1[:,i]))
    lowest_A2 = float(min(list_A2[:,i]))
    d_A1 = np.append(d_A1,lowest_A1)
    d_A2 = np.append(d_A2,lowest_A2)
```

APPENDIX D

Electrostatic Potential

The data for the electrostatic potential plots was created using a Siesta post-processing program called Contour. The inputs for Contour are the electrostatic potential file (VH-file) from the Siesta ground-state calculation along with a particular origin for the plot and two spanning vectors for the x and y axis. Since the plots were all in the xy-plane, the origin for Contour was a position in that plane, and the spanning vectors were vectors in the x and y direction. The table below lists the various origins and spanning vectors for each of the eight ZnO surfaces.

The figures below represent the electrostatic potential at various points within the surface of ZnO. For slabs 1-4 the plots represent the potential just within the top layer of ZnO, where the exact z-coordinates of the plane are stated in the caption. For slabs 5-8, the plots showcase the change in electrostatic potential between the uppermost surface of the slab and the surface of the edge defect. For slabs 5-8, the most interesting area of each slab was within the edge defect, so electrostatic potential plots lower than the edge defect are not as significant.

Slab	Origin point	x-axis	y-axis
S1	(-2.75, 2.3)	(-12, 0, 0)	(0, -13.3, 0)
S2	(-2.75, 2.3)	(-12, 0, 0)	(0, -13.3, 0)
S3	(0, 1.9)	(-17, 0, 0)	(0, -13, 0)
S4	(0, 1.9)	(-17, 0, 0)	(0, -13, 0)
S5	(0, -6.3)	(20.46, 0, 0)	(0, -18.5, 0)
S6	(0, 0)	(20.46, 0, 0)	(0, -26, 0)
S7	(5.9, 0)	(30.46, 0, 0)	(0, -30, 0)
S8	(0, 0)	(20.46, 0, 0)	(0, -20, 0)

Table D.1: Table states the origin of the xy-plane and spanning vectors for the x and y axis of the electrostatic potential plots. All units in Å
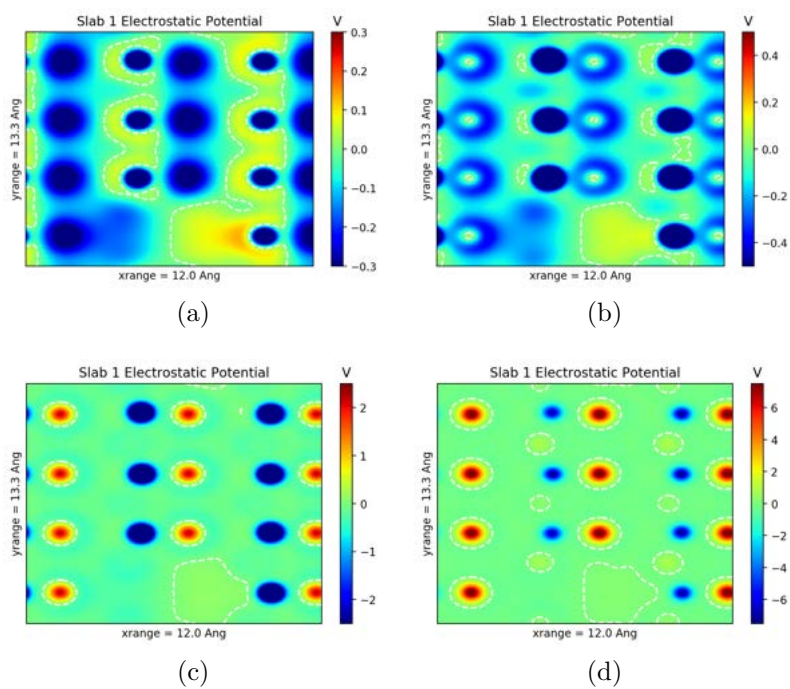
Figure D.1: Slab 1 electrostatic potential. Z value from top left to bottom right: -0.3,-0.6,-0.9,-1.2
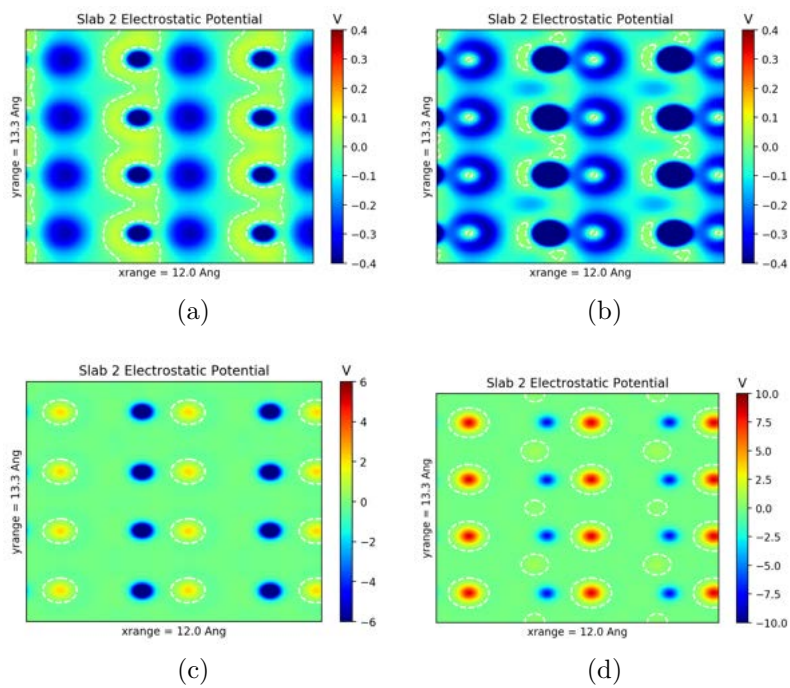
Figure D.2: Slab 2 electrostatic potential. Z value from top left to bottom right: -0.3,-0.6,-0.9,-1.2
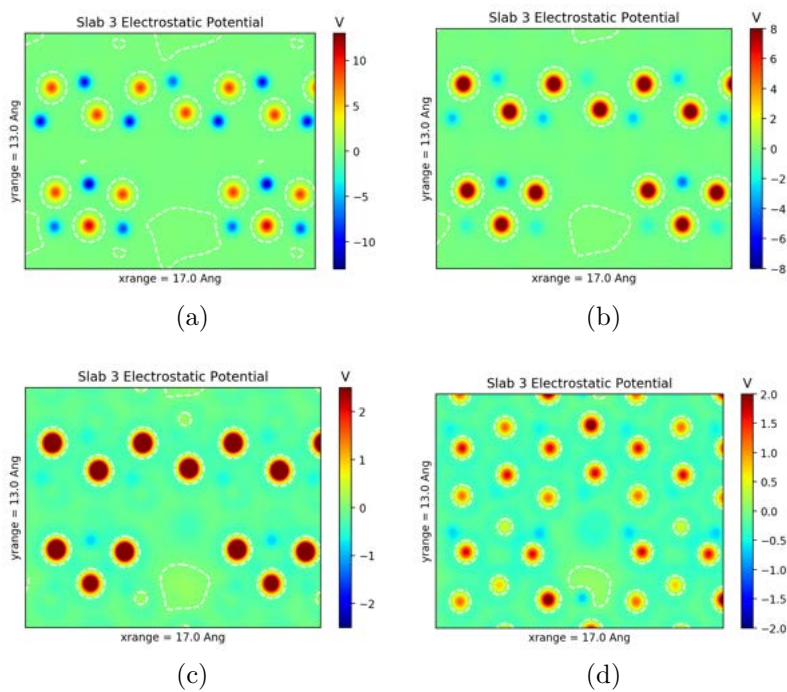
Figure D.3: Slab 3 electrostatic potential. Z value from top left to bottom right: 0.4,0.1,-0.2,-0.5
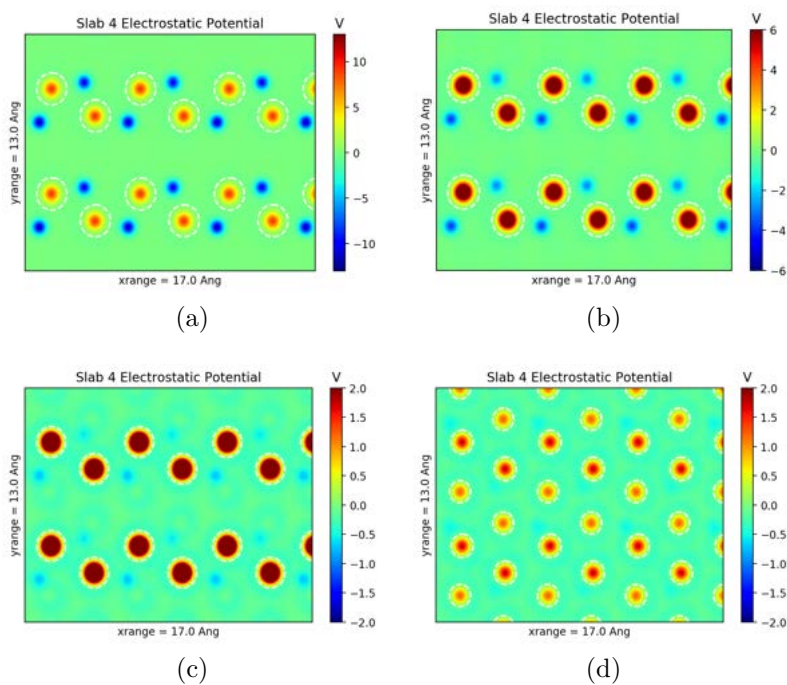
Figure D.4: Slab 4 electrostatic potential. Z value from top left to bottom right: 0.4,0.1,-0.2,-0.5
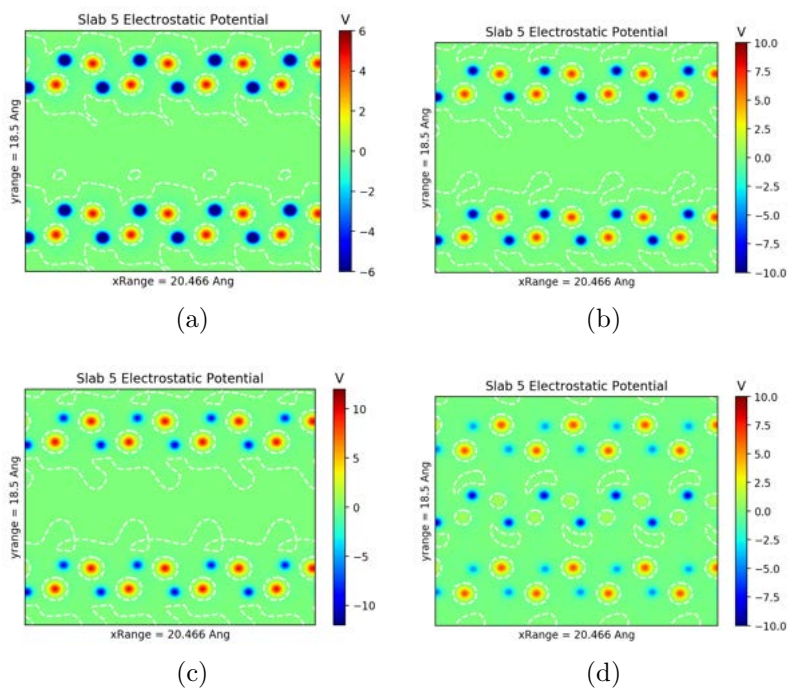
Figure D.5: Slab 5 electrostatic potential. Z value from top left to bottom right: 0.6,0.5,0.4,0.3
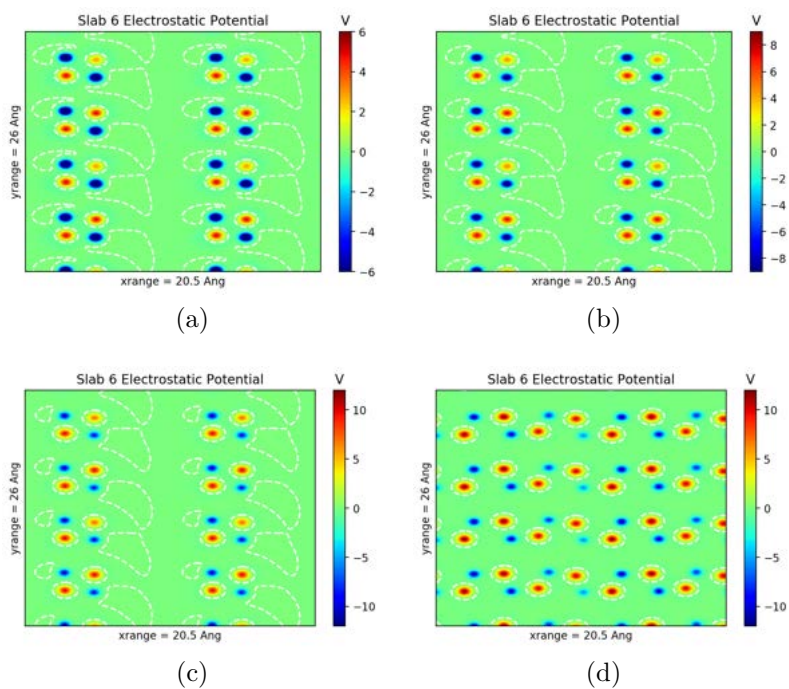
Figure D.6: Slab 6 electrostatic potential. Z value from top left to bottom right: 0.6,0.5,0.4,0.3
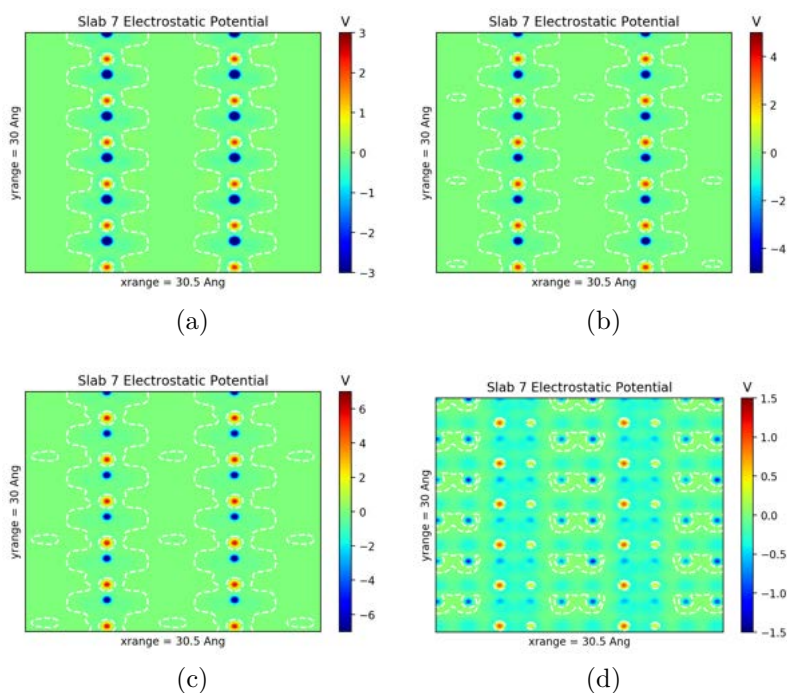
Figure D.7: Slab 7 electrostatic potential. Z value from top left to bottom right: 0.4,0.3,0.2,0.1
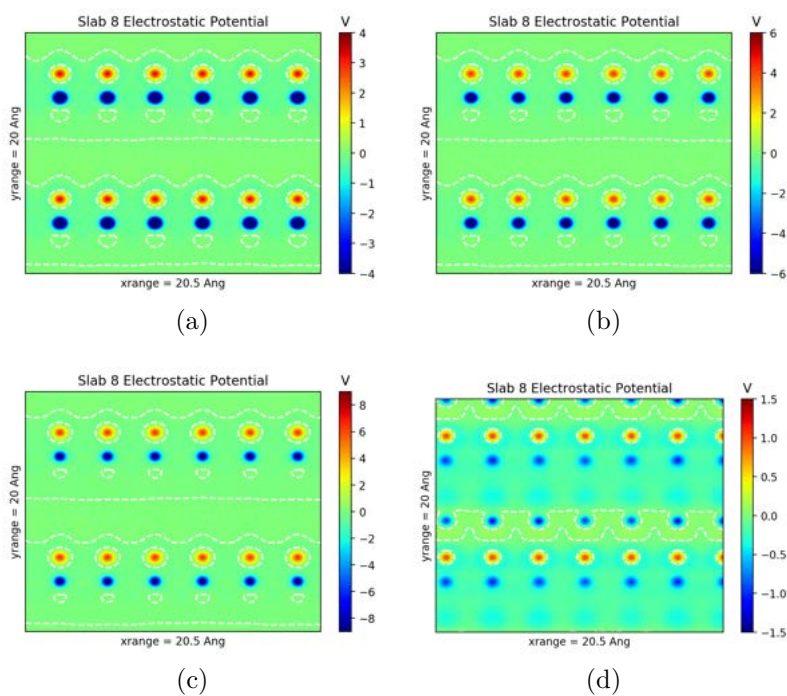
Figure D.8: Slab 8 electrostatic potential. Z value from top left to bottom right: 0.4,0.35,0.3,0.2

APPENDIX E

Additional MD Data

The following plots represent all the data not presented in the body of this paper. The data included in the body represent the most interesting results from the extensive amount of MD calculations done. All the rest of the data is stated below:
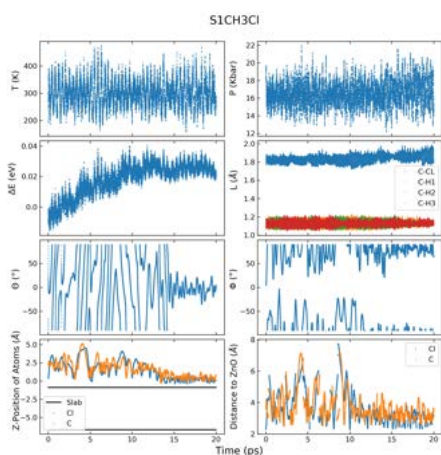
Figure E.1: S1 CH$_3$Cl MD Data
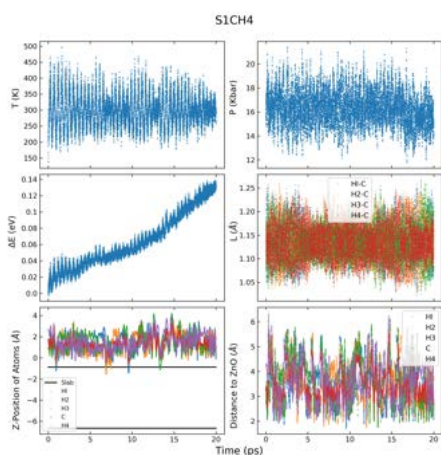
Figure E.2: S1 CH$_4$ MD Data
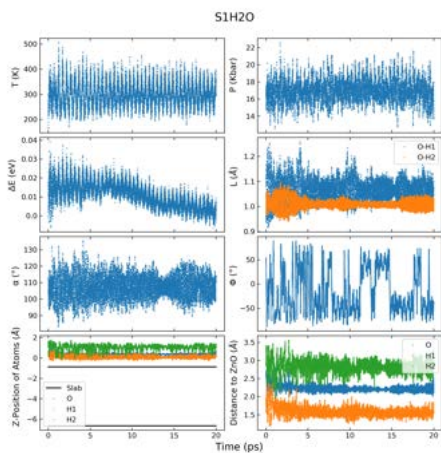
Figure E.3: S1 H$_2$O MD Data
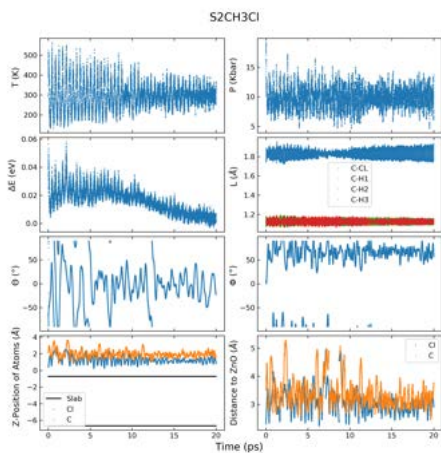
Figure E.4: S2 CH$_3$Cl MD Data
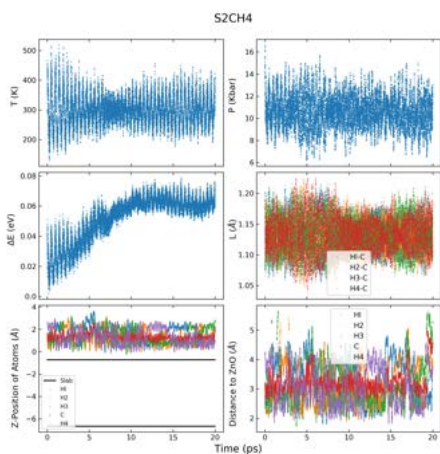
Figure E.5: S1 CH$_4$ MD Data
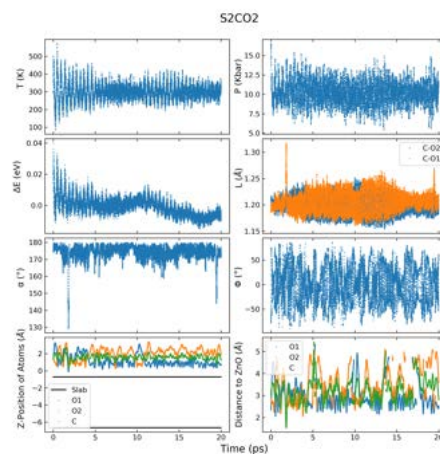
Figure E.6: S2 CO$_2$ MD Data
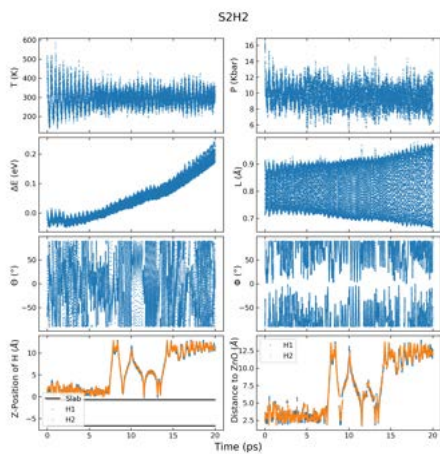
Figure E.7: S1 H$_2$ MD Data
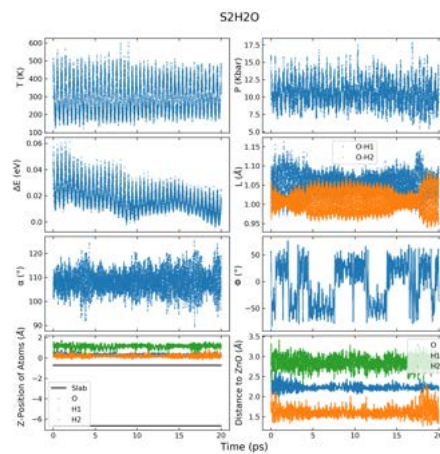
Figure E.8: S2 H$_2$O MD Data
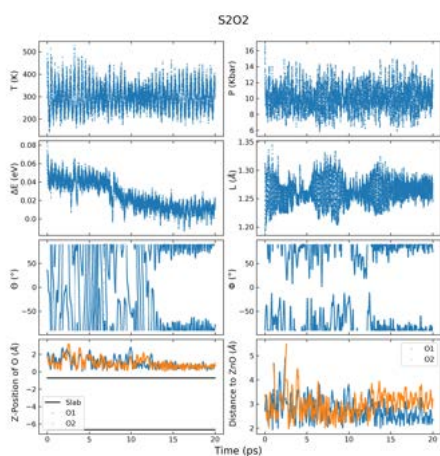
Figure E.9: S2 O$_2$ MD Data
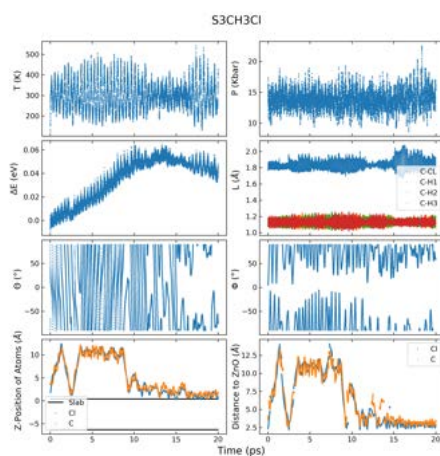
Figure E.10: S3 CH$_3$Cl MD Data
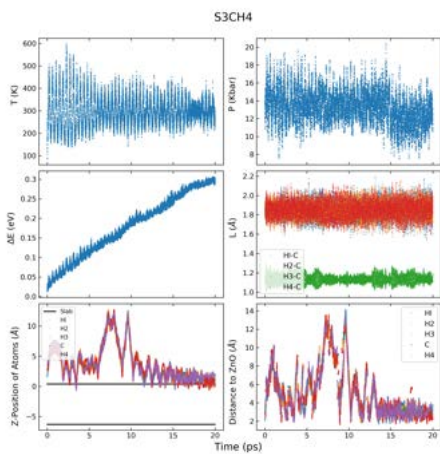
Figure E.11: S2 CH$_4$ MD Data
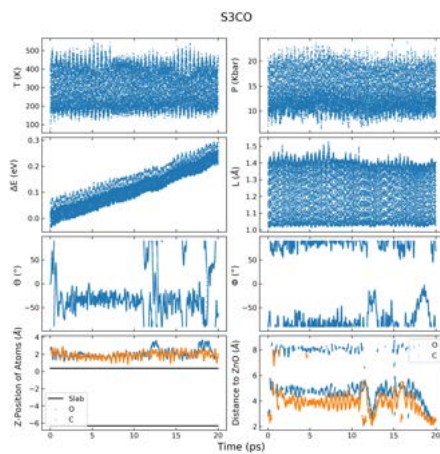
Figure E.12: S3 CO MD Data
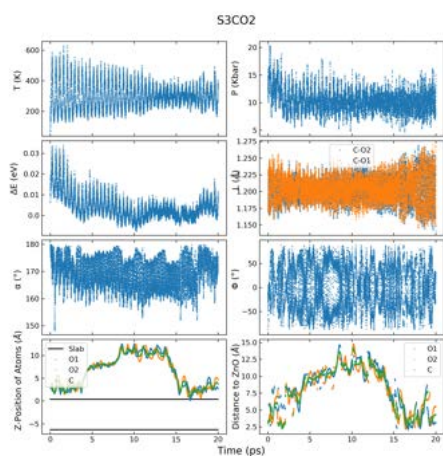
Figure E.13: S3 CO$_2$ MD Data
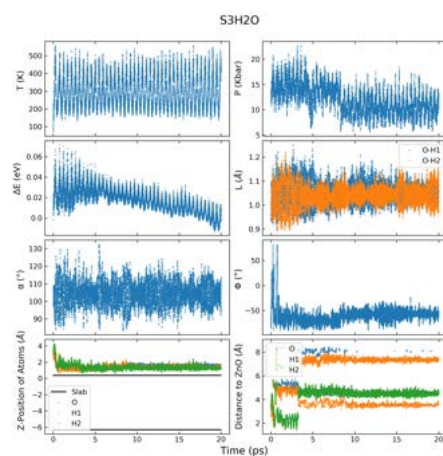
Figure E.14: S3 H$_2$O MD Data
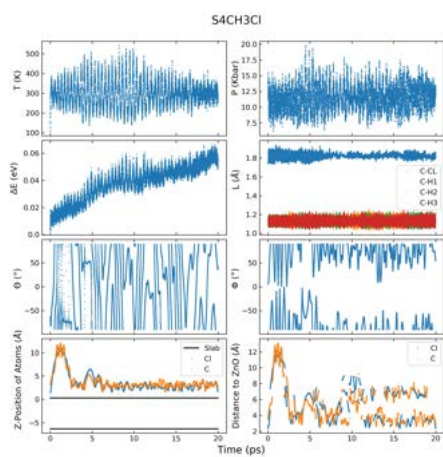
Figure E.15: S4 CH$_3$Cl MD Data
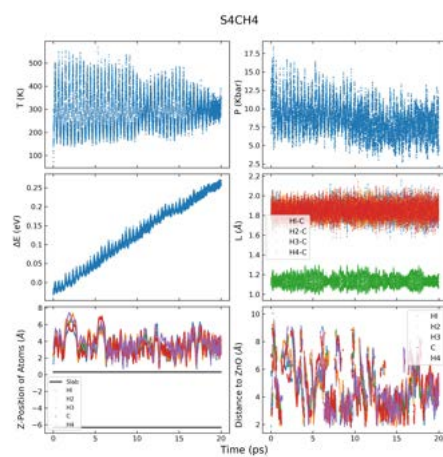
Figure E.16: S4 CH$_4$ MD Data
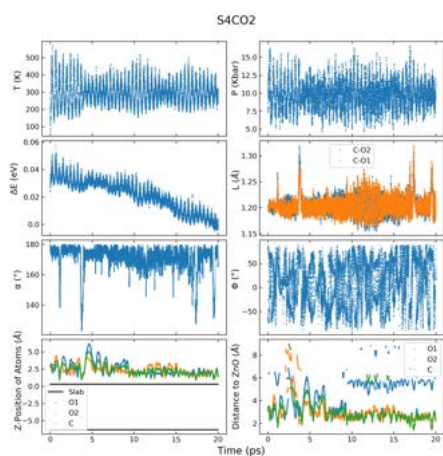
Figure E.17: S4 CO$_2$ MD Data
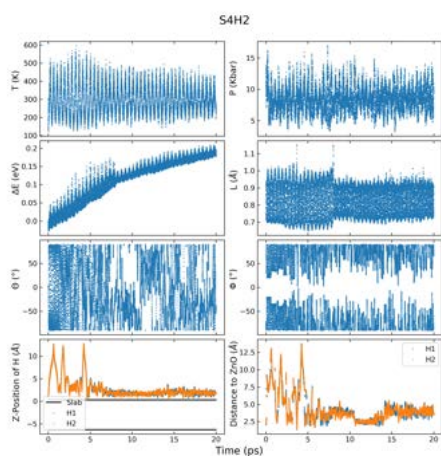
Figure E.18: S4 H$_2$ MD Data
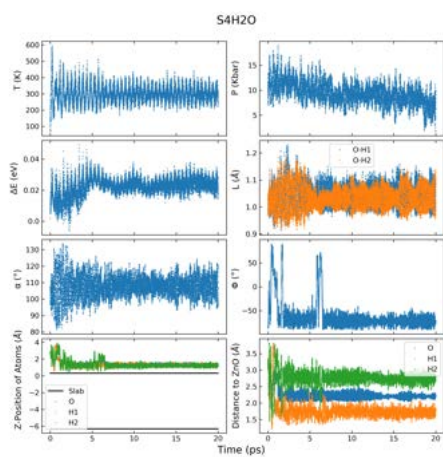
Figure E.19: S4 H$_2$O MD Data
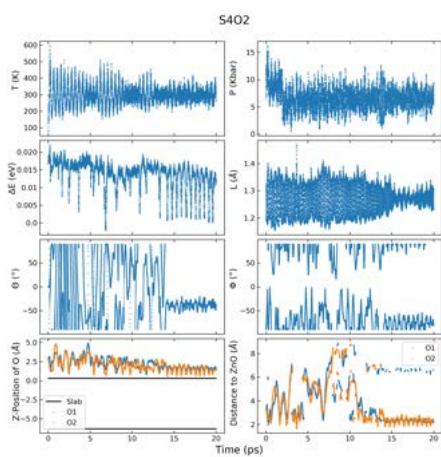
Figure E.20: S4 O$_2$ MD Data
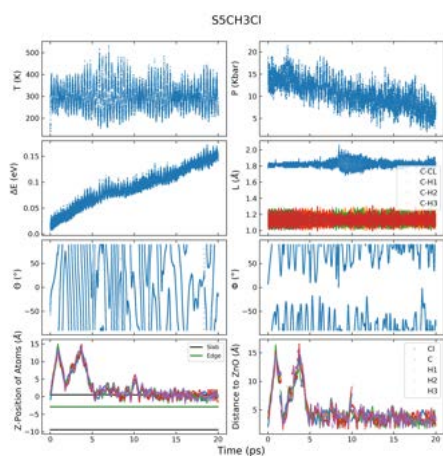
Figure E.21: S5 CH₃Cl MD Data
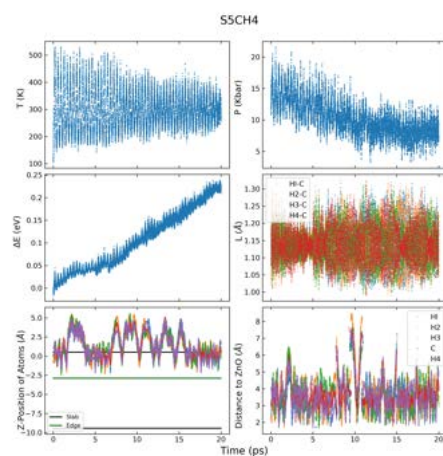
Figure E.22: S5 CH₄ MD Data
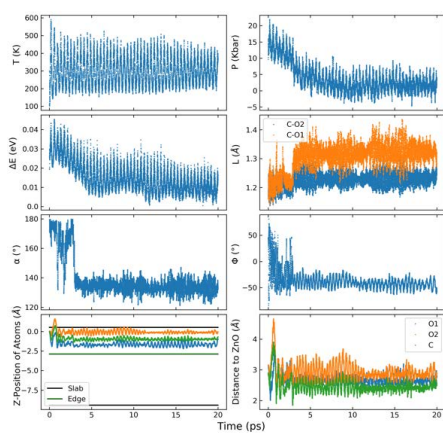
Figure E.23: S5 CO₂ MD Data
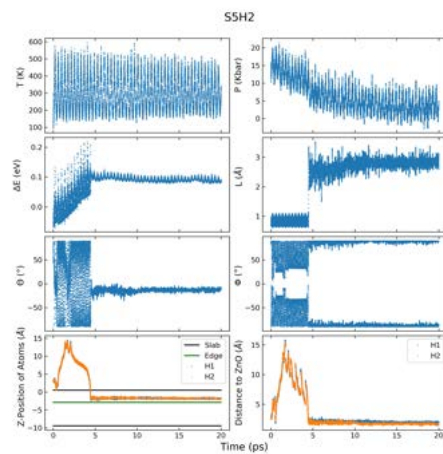
Figure E.24: S5 H₂ MD Data
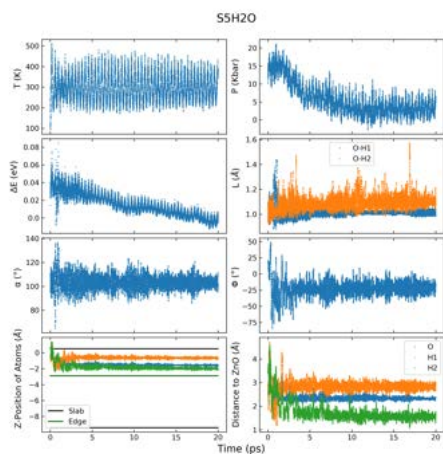
Figure E.25: S5 H$_2$O MD Data
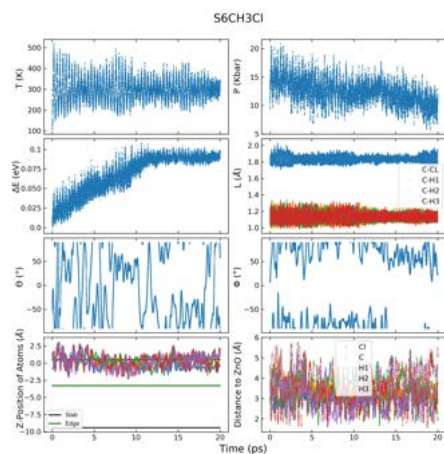
Figure E.26: S6 CH$_3$Cl MD Data
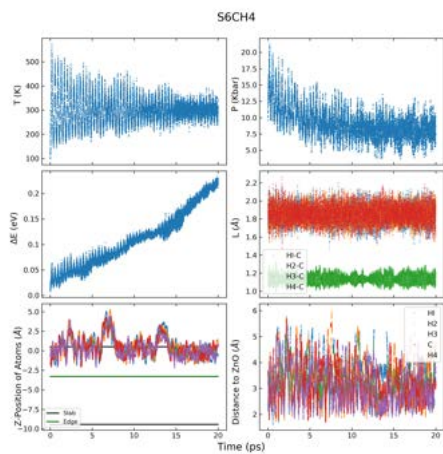
Figure E.27: S6 CH$_4$ MD Data
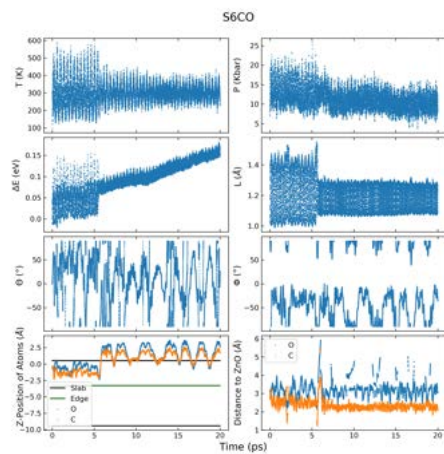
Figure E.28: S6 CO MD Data
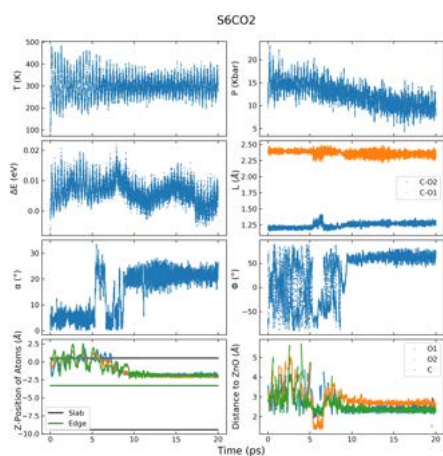
Figure E.29: S6 CO$_2$ MD Data
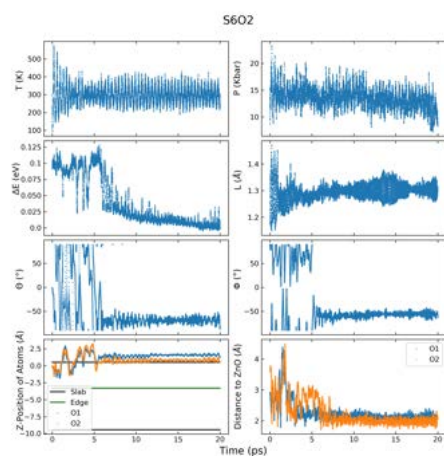
Figure E.30: S6 O$_2$ MD Data
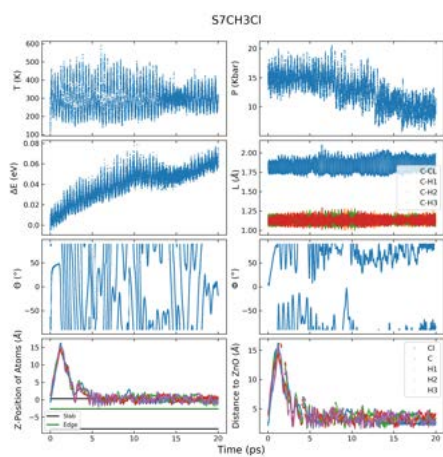
Figure E.31: S7 CH$_3$Cl MD Data
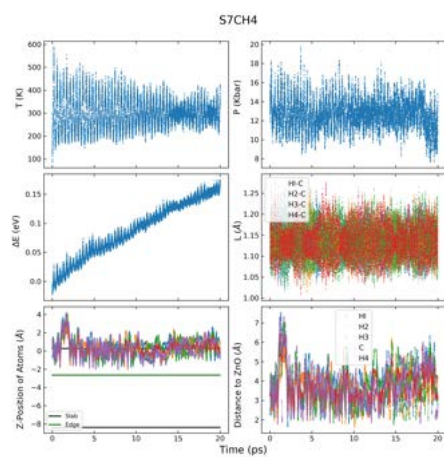
Figure E.32: S7 CH$_4$ MD Data
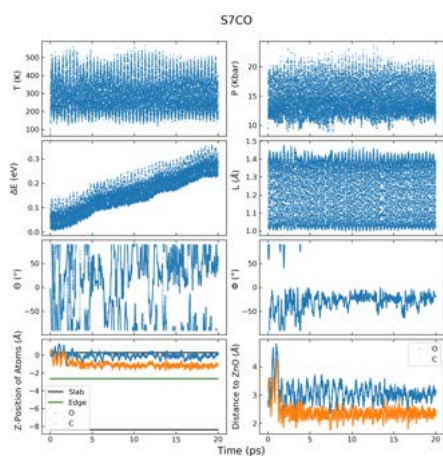
Figure E.33: S7 CO MD Data
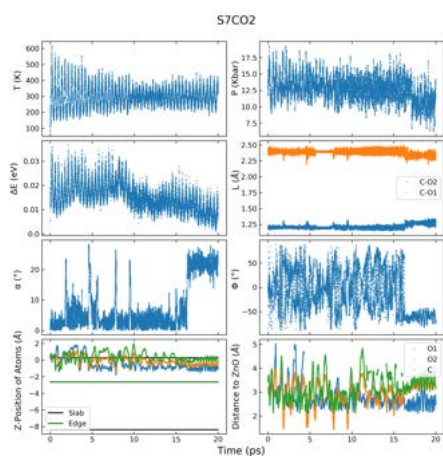
Figure E.34: S7 CO$_2$ MD Data
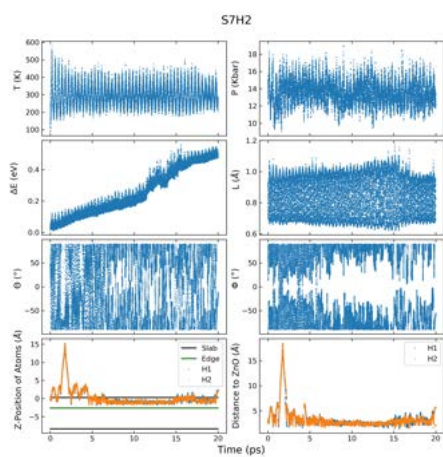
Figure E.35: S7 H$_2$ MD Data
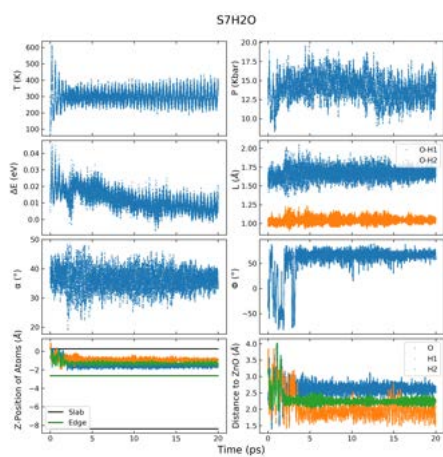
Figure E.36: S7 H$_2$O MD Data
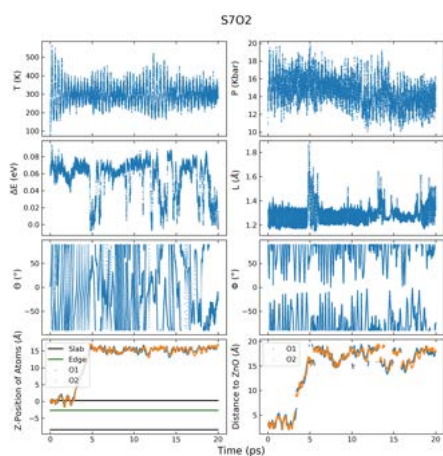
Figure E.37: S7 O$_2$ MD Data
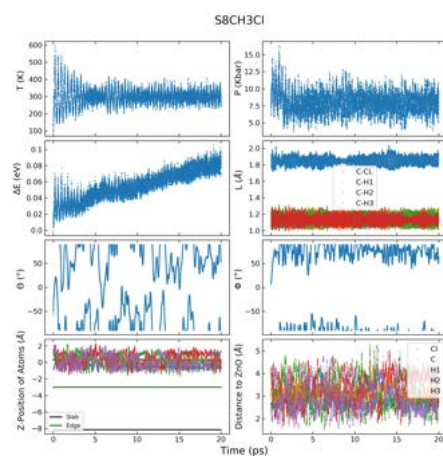
Figure E.38: S8 CH$_3$Cl MD Data
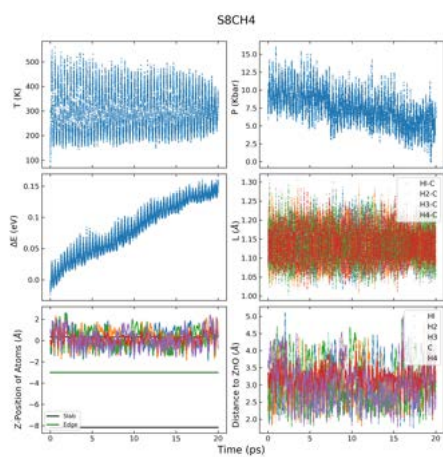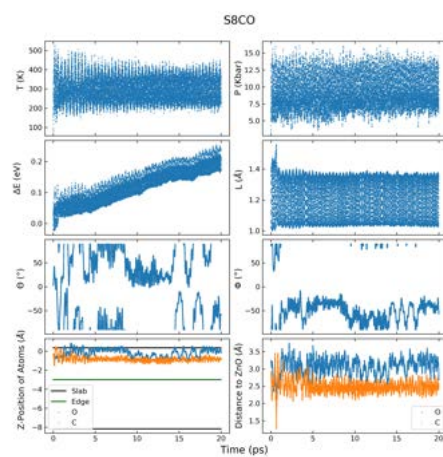

Figure E.39: S8 CH$_4$ MD Data

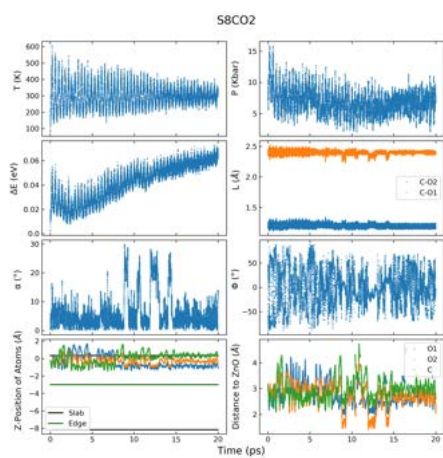
Figure E.40: S8 CO MD Data
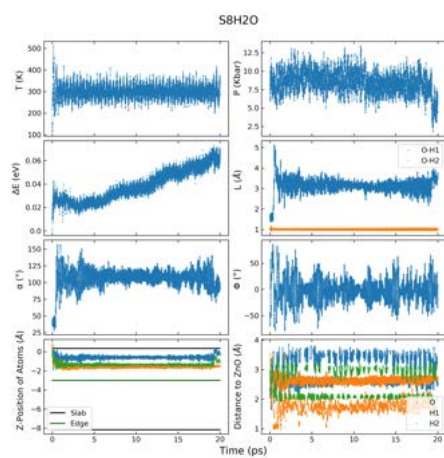
Figure E.41: S8 CO$_2$ MD Data

Figure E.42: S8 H$_2$O MD Data

VITA

CHARITH R. DESILVA

Candidate for the Degree of

Masters of Science

Thesis: ASSESSING THE POTENTIAL OF ZNO SURFACES FOR FISCHER-TROPSCH SYNTHESIS USING CAR-PARRINELLO MOLECULAR DYNAMICS

Major Field: Physics

Biographical:

Education:
Completed the requirements for the degree of Masters of Science with a major in Physics at Oklahoma State University, Stillwater, Oklahoma in December 2020.
Received a Bachelors of Science in Physics at Oklahoma State University, Stillwater, Oklahoma in May 2018.

Experience:
Graduate Teaching Assistant 2018-2020
Graduate Research Assistant May 2020 - August 2020

Professional Affiliations:
Phi Kappa Phi